Available online at www.sciencedirect.com

ScienceDirect

Geochimica et Cosmochimica Acta 314 (2021) 27–54

Geochimica et Cosmochimica Acta

www.elsevier.com/locate/gca

Structure and properties of alkali aluminosilicate glasses and melts: Insights from deep learning

Charles Le Losq [a,b,c,*], Andrew P. Valentine [b,d], Bjorn O. Mysen [c], Daniel R. Neuville [a]

[a] Université de Paris, Institut de physique du globe de Paris, CNRS-UMR 7154, Paris 75005, France
[b] Research School of Earth Sciences, Australian National University, Canberra 2601, Australia
[c] Earth Planets Laboratory, Carnegie Institution for Science, Washington D.C. 20001, USA
[d] Department of Earth Sciences, Durham University, South Road, Durham DH1 3LE, UK

Received 2 April 2021; accepted in revised form 19 August 2021; Available online 28 August 2021

Abstract

Aluminosilicate glasses and melts are of paramount importance for geo- and materials sciences. They include most magmas, and are used to produce a wide variety of everyday materials, from windows to smartphone displays. Despite this importance, no general model exists with which to predict the atomic structure, thermodynamic and viscous properties of aluminosilicate melts. To address this, we introduce a deep learning framework, 'i-Melt', which combines a deep artificial neural network with thermodynamic equations. It is trained to predict 18 different latent and observed properties of melts and glasses in the K_2O-Na_2O-Al_2O_3-SiO_2 system, including configurational entropy, viscosity, optical refractive index, density, and Raman signals. Viscosity can be predicted in the 10^0–10^{15} $\log_{10}$ Pa·s range using five different theoretical frameworks (Adam-Gibbs, Free Volume, MYEGA, VFT, Avramov-Milchev), with a precision equal to, or better than, 0.4 $\log_{10}$ Pa·s on unseen data. Density and optical refractive index (through the Sellmeier equation) can be predicted with errors equal or lower than 0.02 and 0.006, respectively. Raman spectra for K_2O-Na_2O-Al_2O_3-SiO_2 glasses are also predicted, with a relatively high mean error of ~25% due to the limited data set available for training. Latent variables can also be predicted with good precisions. For example, the glass transition temperature, T_g, can be predicted to within 19 K, while the melt configurational entropy at the glass transition, $S^{conf}(T_g)$, can be predicted to within 0.8 J mol^{-1} K^{-1}.

Applied to rhyolite compositions, i-Melt shows that the rheological threshold separating explosive and effusive eruptions correlates with an increase in the fraction of non-bridging oxygens in rhyolite melts as their alkali/Al ratio becomes larger than 1. Exploring further the effect of the K/(K + Na) ratio on the properties of alkali aluminosilicate melts with compositions varying along a simplified alkali magmatic series trend, we observe that K-rich melts have systematically different structures and higher viscosities compared to Na-rich melts. Combined with the effects of the K/(K + Na) ratio on other parameters, such as the solubility, solution mechanisms and speciation of volatile elements, this could ultimately influence the eruptive dynamics of volcanic systems emitting Na-rich or K-rich alkali magmas.

Keywords: Aluminosilicate melt; Glass; Machine learning; Viscosity; Thermodynamic properties; Magma; Volcanology; grey-box neural networks

1. INTRODUCTION

How do molten silicates move? How do they exchange heat with other media? How do they crystallize? Questions such as these underpin many practical problems, ranging

* Corresponding author at: Université de Paris, Institut de physique du globe de Paris, CNRS-UMR 7154, Paris 75005, France.
E-mail address: lelosq@ipgp.fr (C. Le Losq).

https://doi.org/10.1016/j.gca.2021.08.023
0016-7037/

from the dynamics of volcanic eruptions (Dingwell, 1996) and the formation of igneous rocks (Bowen, 1928), to the manufacture of novel glass, glass–ceramic and ceramic materials, including the development of enhanced technological glass materials suitable for smartphone screens (Varshneya and Bihuniak, 2017). To address such questions, knowledge of melt and glass physical properties, such as viscosity, heat capacity and entropy, is necessary. These properties, in turn, are ultimately governed by the liquid's composition and, therefore, atomic/ionic structure (see for reviews Le Losq et al., 2019b; Mysen and Richet, 2019). Some properties, such as silicate melt and glass heat capacity, can be predicted reasonably well with existing models (e.g., see for heat capacity Stebbins et al., 1984; Richet and Bottinga, 1985; Richet, 1987; Tangeman and Lange, 1998; Webb, 2008; Giordano and Russell, 2017). However, other properties are more difficult to model. This includes viscosity, because of its complex dependence on temperature and melt composition. Silicate melt viscosity variations with temperature, *T*, are, in most cases, non-Arrhenian. At constant T, viscosity can exhibit large and non-linear variations with changing melt composition, particularly if T is in the supercooled temperature domain. This domain is located well below the liquidus, close to the glass transition temperature, which separates melts from glasses. Such a situation is unfortunate because viscosity is of great interest: it influences not only volcanic processes (Dingwell, 1996; Papale, 1999; Gonnermann and Manga, 2013; Gonnermann, 2015; Cassidy et al., 2018), but also glass-forming processes in the glass manufacturing industry.

Currently, predictions of a property such as viscosity rely on (i) empirical models, (ii) thermodynamic models, or (iii) molecular dynamics (MD) simulations. Empirical models are interpolative in nature, and bring no information about the links between structural, thermodynamic and dynamic properties of silicate melts. They can be sufficiently precise to accurately predict some properties, such as the glass and melt heat capacities (Stebbins et al., 1984; Richet and Bottinga, 1985; Richet, 1987; Tangeman and Lange, 1998; Russell and Giordano, 2017). In the case of viscosity, empirical models rely on empirical equations (Bottinga and Weill, 1972; Shaw, 1972; Persikov, 1991; Hess and Dingwell, 1996; Hui and Zhang, 2007; Giordano et al., 2008; Duan, 2014), such as the Arrhenius or the Vogel-Fulcher-Tammann (VFT) laws. When compared to experimental results, these empirical models can exhibit poor predictive performance, markedly worse than their initially communicated uncertainties (e.g., Robert et al., 2013; Le Losq and Neuville, 2013; Sehlke and Whittington, 2016; Di Genova et al., 2017). They provide a practical way of making viscosity predictions, but their usefulness is restricted by the chemical composition and temperature range within which the models have been calibrated. In addition, these models do not provide any further information about the flow process.

Thermodynamic models circumvent the shortcomings of empirical models, particularly their interpolative nature and the lack of physical/thermodynamic background that limits understanding of the processes underlying melt flow. Initially, thermodynamic models for viscosity were limited to mixtures of specific melts comprising only a few oxides (e.g., Richet, 1984; Hummel and Arndt, 1985; Neuville and Richet, 1991). Analogous attempts were made to model other properties, such as the model of Mysen (1995) which calculates the configurational heat capacity of silicate melts from their fractions of tetrahedral SiO_4 Q^n units (Q being a tetrahedral unit and n the number of bridging oxygen it carries; *4-n* thus gives the number of non-bridging oxygens). With recent advances in our knowledge of the links between melt structure, thermodynamic properties and viscosity, it has become possible to construct more complex thermodynamic models of the properties of silicate melts, either directly from the melt chemical composition or based on knowledge of their structure. For example, Sehlke and Whittington (2016) proposed a model, based on the Adam-Gibbs theory of relaxation processes (Adam and Gibbs, 1965, see Section 2.5.2), to predict the viscosity of tholeiitic melts with an average error of 0.13 $\log_{10}$ Pa·s, in the 10^0–10^{12} Pa·s range. Le Losq and Neuville (2017) also proposed a model based on the Adam-Gibbs theory of relaxation processes. Their model connects viscosity, heat capacity, configurational entropy, structure and chemical composition for melts in the Na_2O-K_2O-SiO_2 system. In this system, it allows viscosity predictions with an average error lower than 0.2 $\log_{10}$ Pa·s in the 10^0–10^{12} Pa·s range. A third example is the model proposed by Starodub et al. (2019). It combines an associated solution model of melt structure with the Avramov-Milchev equation of viscous flow (Avramov and Milchev, 1988; Avramov, 2011) to predict melt viscosity in the 10^0–10^{12} Pa·s range in the Na_2O-K_2O-Al_2O_3-SiO_2 system.

Structure-thermodynamic models, like those discussed above, can be precise and provide important information about the links between composition, structure and properties. However, such models suffer from an important drawback: a good knowledge of melt structure is required. While this can be achieved for silicate melts through, for instance, ^{29}Si Nuclear Magnetic Resonance (NMR) spectroscopy (e.g., Maekawa et al., 1991), such information is more difficult to obtain for aluminosilicate compositions. In such compositions, Si-Al interactions broaden the ^{29}Si NMR signal, and hence retrieving the Q^n speciation is not routine: it relies on various assumptions required for modeling the ^{29}Si NMR spectra (e.g., see the studies of Mysen et al., 2003; Diallo et al., 2019; Sreenivasan et al., 2020). Critical pieces of information are obtained through ^{17}O NMR spectroscopy (e.g., Lee and Stebbins, 2009; Lee et al., 2016) but do not directly provide information about the Q^n speciation used in existing structural-thermodynamic models (e.g., Le Losq and Neuville, 2017; Starodub et al., 2019). Raman spectroscopy may also be used (McMillan, 1984; Matson and Sharma, 1985; Merzbacher and White, 1991; Mysen, 1999), as shown by successful results for alkali silicate and aluminosilicate glasses (Mysen, 1990, 2007; Mysen and Frantz, 1992; Neuville and Mysen, 1996; Malfait et al., 2007; Zakaznova-Herzog et al., 2007; Koroleva et al., 2013; Nesbitt et al., 2021). However, the variations of the Raman peak cross sections, which are needed to convert Raman peak areas into Q^n unit fractions, are not known as well as would be desired. Furthermore, the peak-fitting

protocols can be subject to discussion, as shown by a lack of consensus visible when comparing different studies (e.g., compare the methods described in the studies of Mysen et al., 1982a; Mysen, 1990; You et al., 2005; Malfait, 2009; Le Losq and Neuville, 2013; Le Losq et al., 2014; Bancroft et al., 2018; Nesbitt et al., 2019, 2021). In any case, models that only rely on Q^n fractions are incomplete because many other structural details affect the properties of aluminosilicate melts. These include, but are not limited to, changes in Al coordination with composition, temperature and pressure (Stebbins et al., 2000, 2008; Toplis et al., 2000; Allwardt et al., 2005a, b; Kiczenski et al., 2005; Neuville et al., 2006, 2007, 2008a,b; Massiot et al., 2008; Lee et al., 2012; Le Losq et al., 2014; Morin et al., 2014; Park and Lee, 2014; Drewitt et al., 2015; Lee et al., 2020), Al-Si ordering between tetrahedral units (Lee and Stebbins, 1999; Lee, 2005; Lee et al., 2016; Allu et al., 2018), or excess non-bridging oxygens (Stebbins and Xu, 1997; Stebbins et al., 1999; Oglesby et al., 2002; Iuga et al., 2005; Thompson and Stebbins, 2011, 2012, 2013; Xiang et al., 2013). The complexity of the atomic structure of melts and glasses is thus very high. Because of this, developing thermodynamic models to predict the properties of multicomponent magmatic and industrial melt/glass compositions is a difficult task.

MD simulation (Rapaport, 2004) is another pathway that allows us to infer the structure and properties of complex melts. Such models bring important structural, dynamic and thermodynamic information by simulating atomic movements at sub-microsecond timescales (Guillot and Sator, 2007; Vuilleumier et al., 2009; Bauchy et al., 2013; Wang et al., 2014; Dufils et al., 2017, 2020). They provide models that can be used to assess how melt behaves at temperatures typically higher than 2000 K, how atoms move and interact, and how this affects their physical properties such as viscosity and density. While such predictions are very informative about processes at super-liquidus conditions and can be useful for high-temperature applications (e.g., modeling conditions in glass furnaces or planetary magma oceans), they are less helpful at lower temperatures, for example in the 700–1300 °C temperature range typical of volcanic eruptions. Furthermore, MD simulation simulates the system on very short timescales, typically less than a microsecond for classical MD models, with even shorter timescales for *ab initio* calculations. This is far removed from glass-making conditions and from volcanological timescales, which range from minutes to several thousands of years and beyond.

In this study, we explore the use of an interesting method for structural, thermodynamic and dynamic property predictions: semiphysical neural networks also known as grey-box neural networks (GBNN). These combine physical equations with artificial neural networks, bringing advantages in comparison to both traditional physical/thermodynamic models and "pure" machine learning models. GBNNs leverage our current knowledge of physical systems by integrating existing physical equations, but add the power of machine learning to infer connections between variables not yet understood theoretically – for instance, between glass chemical composition and configurational entropy. GBNNs have been successful in many applications (Willard et al., 2020), including the analysis of seismic waveforms (e.g., Moseley et al., 2020; Smith et al., 2020) and lake temperature modeling (Karpatne et al., 2018). This has inspired recent efforts to model the viscosity of ionic liquids with neural networks (Paduszyński and Domańska, 2014; Beckner et al., 2018). For silicate melts, there have been several attempts to predict melt and glass properties using machine learning (see the reviews of Tandia et al., 2019; Liu et al., 2019), stretching back to the work of Dreyfus and Dreyfus (2003) on the prediction of liquidus temperature with artificial neural networks. Regarding melt viscosity, Hwang et al. (2020) recently proposed an approach based on machine learning and the use of "cationic fingerprinting" to predict the temperatures of three reference viscosity points ($10^{1.5}$, $10^{6.6}$ and 10^{12} Pa·s) for Na_2O-SiO_2-Al_2O_3-CaO melts with an error of ±33 °C. Cassar (2021) also proposed the ViscNet model, a GBNN model that combines either the VFT or the MYEGA viscosity equations (see Section 2.5.2) with a neural network to perform viscosity predictions of silicate and aluminosilicate melts. Such results are very encouraging and showcase the ability of GBNN to provide pragmatic, practical models for property predictions.

Here, we go a step further by presenting a GBNN model ("i-Melt") that combines several physical equations with a deep learning neural network, and predicts many different melt and glass properties of interest for geology and industry. This includes melt viscosity, glass transition temperature, fragility and configurational entropy – all important properties defining the mobility of the melt – as well as the density and optical refractive index of glasses, which are of interest for industrial applications. We also predict Raman spectra, which are readily-observed and provide information about the atomic structure of the glass. Other properties, such as thermal expansion coefficients, can be of interest but were left out of the modeling at this stage. i-Melt is thus a GBNN "multitask" model, which has the ability to predict different features/properties of the same object: a silicate melt/glass. i-Melt was trained on melt and glass compositions in the K_2O-Na_2O-Al_2O_3-SiO_2 system, for which a fairly complete, albeit sparse, experimental dataset is available. In this system, i-Melt allows systematic exploration of the links between melt/glass composition, structure and properties, as we describe below. Building on this, we are then able to comment on the source of the compositional control on eruptive dynamics observed for rhyolite melts, as well as on the possible importance of the K/(K + Na) ratio in alkaline magmatic series.

2. METHODS

2.1. Experimental Design

The development of the deep learning model requires the collection and compilation of viscosity, density, refractive index data, and Raman spectra for glasses and melts in the K_2O-Na_2O-Al_2O_3-SiO_2 quaternary system (Fig. 1). The viscosity of supercooled melts for peralkaline compositions in this system is not well understood, and

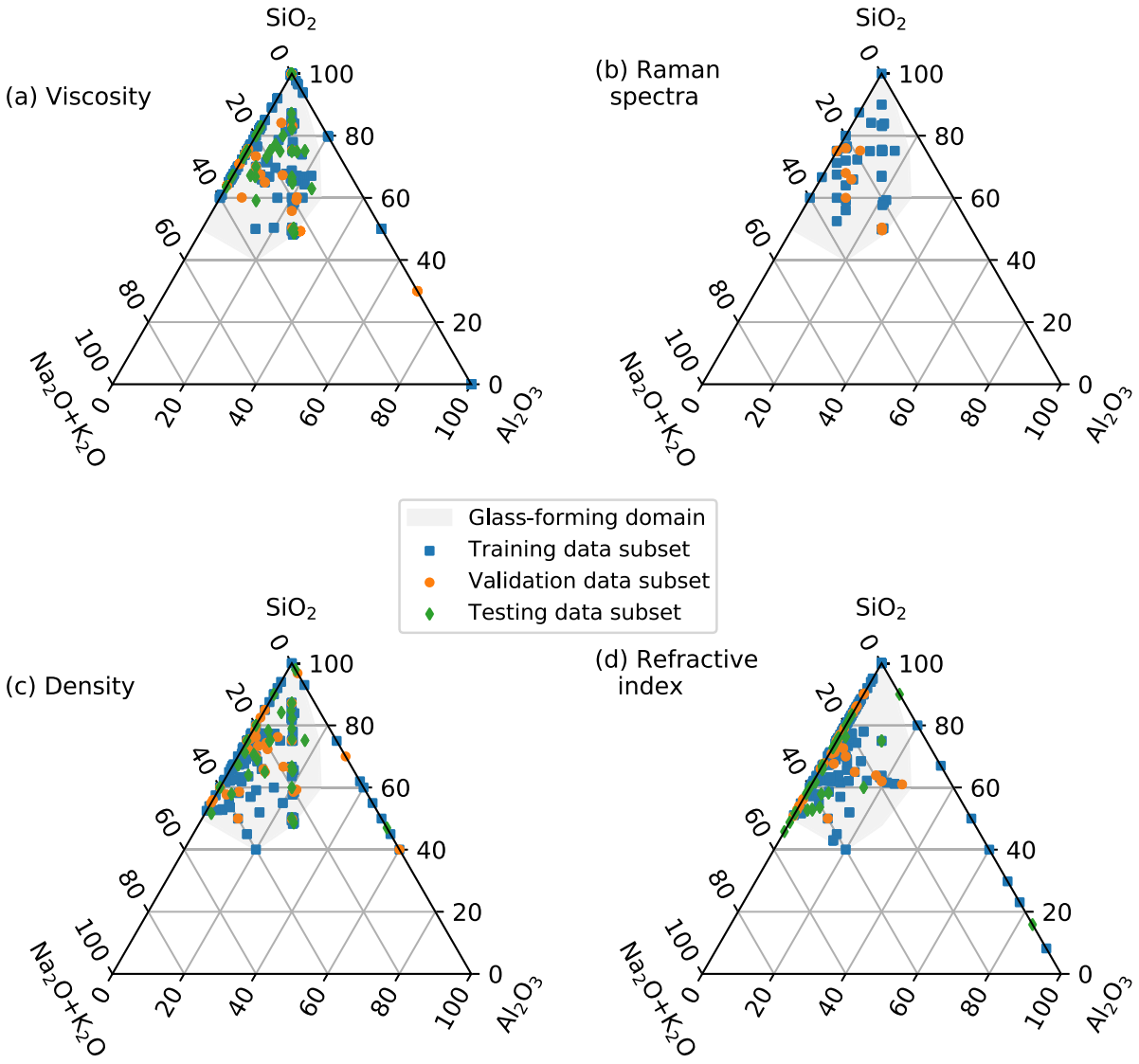

Fig. 1. Datasets for melt viscosity (a), glass Raman spectroscopy (b), glass density (C) and glass refractive index (d). Each symbol corresponds to a sample. The glass-forming domain at usual laboratory cooling rates is indicated in grey.

we conducted additional experiments to complement the existing dataset. We further compiled existing data as specified below, prior to developing the i-Melt framework in the Python programming language, by using the PyTorch library. All code and data necessary to reproduce this study are available from Github at https://github.com/charlesll/i-melt; future improvements will be also distributed via this repository.

2.2. Datasets

Existing Raman spectra and observations of optical refractive index, density and viscosity of alkali aluminosilicate glasses were selected by hand via a review of the existing literature. Validation of the accuracy of viscosity data across different studies is critical and was checked on melt compositions including $Na_2Si_3O_7$, $NaAlSi_3O_8$ and $NaAlSi_2O_6$. We plotted all the literature data for such compositions, and observed the mean trend of these data. Most data fall within 0.1 $\log_{10}$ Pa·s, forming a clear general trend. Published data with deviations larger than 0.1 $\log_{10}$ Pa·s compared to this general trend were discarded. Density and refractive index come from various publications, in particular from publications reviewed in Mazurin et al. (1987). Raman spectra were published data from the IPGP and Carnegie Institution for Science laboratories (see below for details). All the data and their sources are provided in the database available in the software repository. We thus have four different streams of data:

– $D_{viscosity}$, the dataset of melt viscosity measurements, composed of $X_{viscosity}$ chemical composition entries (mole fractions) as well as their associated temperatures (Kelvin) and $y_{viscosity}$ observations ($\log_{10}$ Pa·s);

- $D_{density}$, the dataset of glass density measurements, composed of $X_{density}$ chemical composition entries (mole fractions) and $y_{density}$ observations (g cm^{-3});
- D_{Raman}, the dataset of glass Raman spectra, composed of X_{Raman} chemical composition entries (mole fractions) and y_{Raman} spectra observations (normalised Raman intensities);
- $D_{optical}$, the glass dataset of optical refractive index, composed of $X_{optical}$ chemical composition entries (mole fractions) as well as their associated wavelength (μm) and $y_{refractive\ index}$ observations.

$D_{viscosity}$, $D_{density}$ and $D_{optical}$ cover an important part of the glass-forming domain of alkali aluminosilicates (Fig. 1). These data were, thus, used to train the artificial neural network with a "performance oriented" mindset, i.e. we want the model predictions to be as accurate as possible. D_{Raman} covers a more limited set of compositions (Fig. 1). It was used as a way of improving multitask learning: achieving inductive transfer between related tasks using a shared representation of the problem (Caruana, 1997). Multitask learning is known to generally improve the performance of learning. Here, Raman spectra encode structural information that could assist the network in learning physical properties, embedding a shared representation of the composition-structure–property links in melts and glasses.

2.3. Sample synthesis and viscosity-density measurements

To extend the viscosity dataset for peralkaline aluminosilicate melts, additional compositions were synthesized at IPGP in Paris from reagent-grade K_2CO_3, Na_2CO_3, Al_2O_3 and SiO_2 dried oxide powders, following the protocol described in Le Losq and Neuville (2013). Viscosity and density measurements follow the protocol used in the Geomaterials laboratory at IPGP (Neuville, 2006; Le Losq and Neuville, 2013; Le Losq et al., 2014). Chemical compositions (Table 1) have been measured using a Cameca SX50 electron microprobe, with a 30nA current, U = 30 kV, and 5 seconds of counting. Beam-induced alkali loss was minimized by working with a defocused beam that was moved continuously during the analysis. The mean and standard deviation values reported in Table 1 are calculated from 10 to 20 individual measurements on each sample. The corresponding viscosity measurements are provided in Table 2, and are affected by an error less than or equal to 0.03 $\log_{10}$ Pa·s. All measured viscosities were Newtonian – no dependence on the strain rate was observed.

2.4. Raman spectroscopy

Raman spectra of silicate and aluminosilicate glasses acquired at IPGP (Paris, France) were recorded using a T64000 Jobin-Yvon® Raman spectrometer equipped with a confocal system, a 1024 × 1024 charge-coupled detector (CCD) cooled by liquid nitrogen and an Olympus® microscope. The optimal spatial resolution allowed by the confocal system is 1–2 μm^2 with a 100 × Olympus® objective, and the spectral resolution is 0.7 cm^{-1}. A Coherent® laser 70-C5 Ar^+, having a wavelength of 488.1 or 514.532 nm, has been used as the excitation line. Unpolarized Raman spectra that were excited with a laser power of 100–150 mW on the sample were acquired between 20 and 1500 cm^{-1} on pieces of glass from the starting materials.

Additional Raman spectra acquired at the Geophysical Laboratory on glasses along the $Na_2Si_4O_9$-$Na_2(NaAl)_4O_9$ and $K_2Si_4O_9$-$K_2(KAl)_4O_9$ joins, previously published in Mysen (1996, 1999), were added to the database. Those spectra were acquired with a Dilor XY confocal microRaman spectrometer equipped with a cryogenic Thompson Model 4000 CCD. The 488 nm line of a SpectraPhysics model 2025 Ar^+ laser operating at several hundred mW at the sample was used for sample excitation.

Table 1
Composition of the synthesized glasses. Nominal (nom.) and analyzed (an.) compositions are reported. Standard deviations on measured values on 10 different spots (for EPMA measurements) or glass chips (for density measurements) are given in parenthesis (1σ confidence interval).

Glass name		%SiO_2	%Al_2O_3	%K_2O	%Na_2O	% total	Density, g cm^{-1}
KA80.05	nom. mol%	80.00	5.00	15.00	0.00		
	nom. wt%	71.40	7.60	21.00	0.00		
	an. wt%	74.8(4)	7.6(1)	15.1(2)	0.00(4)	97.5(1)	2.320(1)
KA72.07	nom. mol%	72.00	7.00	21.00	0.00		
	nom. wt%	61.60	10.20	28.20	0.00		
	an. wt%	61.4(3)	10.2(2)	27.4(3)	0.00(2)	99.0(1)	2.408(1)
KA65.09	nom. mol%	65.00	8.75	26.25	0.00		
	nom. wt%	53.70	12.30	34.00	0.00		
	an. wt%	53.3(5)	12.5(4)	31.7(3)	0.00(3)	97.5(1)	2.451(9)
NA65.09	nom. mol%	65.00	8.75	0.00	26.25		
	nom. wt%	60.79	13.89	0.00	25.32		
	an. wt%	61.7(4)	13.7(2)	0.03(2)	24.5(7)	99.9(2)	2.472(4)
NA58.10	nom. mol%	58.00	10.50	0.00	31.50		
	nom. wt%	53.55	16.45	0.00	30.00		
	an. wt%	54.6(3)	16.4(2)	0.05(2)	28.9(4)	99.9(1)	2.502(5)

Table 2
Viscosity measurements in $\log_{10}$ Pa·s. Errors on viscosity are lower or equal to 0.03 $\log_{10}$ Pa·s.

T, K	KA80.05	T, K	KA72.07	T, K	KA65.09	T, K	NA65.09	T, K	NA58.10
1013.1	9.10	921.5	9.37	941.3	9.55	834.0	9.01	827.3	10.10
1001.8	9.32	891.0	10.17	935.1	9.71	829.0	9.18	836.9	9.73
989.6	9.51	872.0	10.75	919.4	10.13	813.8	9.61	817.6	10.51
981.6	9.78	852.0	11.40	913.6	10.32	803.2	9.94	796.2	11.42
967.6	10.05			898.7	10.78	798.6	10.09	805.7	10.97
949.7	10.50			892.0	10.96	787.5	10.50	847.1	9.36
940.3	10.83			882.1	11.28	779.9	10.81	855.9	9.09
928.2	11.05			867.3	11.86	773.7	11.07	828.3	10.01
918.4	11.32			855.4	12.29	772.9	11.07	834.4	9.81
905.1	11.63					762.6	11.52	787.4	11.80
896.6	11.92					756.3	11.74	777.4	12.36
						752.1	11.95		

Preprocessing of the spectra was kept to minimum: (i) the spectra were corrected for temperature and excitation line effects (see details and references in Le Losq and Neuville, 2013; Le Losq et al., 2014), (ii) the spectra were normalised to their maximum intensity I_{max} such that the intensity in each spectrum varies between 0 and 1 ($I_{normalised} = [I - I_{min}]/[I_{max} - I_{min}]$, with I_{min} the minimum intensity of a spectrum). The 400–1250 cm^{-1} portion of Raman spectra, resampled with a step of 1 cm^{-1}, was retained as different spectra had different starting and ending Raman shift values. After pre-processing, these 400–1250 cm^{-1} portions of the spectra were saved in a HDF5 file for their future use.

2.5. Deep learning model

2.5.1. Overview

The i-Melt framework (Fig. 2) combines a deep artificial neural network with various dynamic and thermodynamic equations. This strategy allows the development of an intelligent model that links different observables from the same object (melt/glass). The artificial neural network is a feed forward network with multiple interconnected hidden layers (Murphy, 2012; Goodfellow et al., 2016). It either predicts directly-observable glass properties including density, refractive index and Raman spectra, or outputs the latent variables (such as configurational entropy, S^{conf}, a property that reflects the melt structure) required to predict properties such as melt viscosity through five theoretical and empirical equations commonly used for reproducing experimentally-observed variations of silicate melt viscosity with temperature: Adam-Gibbs, MYEGA, Avramov-Milchev, Tamman-Vogel-Fulcher and Free Volume Theory. In the next section, we will present the possibility of performing such *trans-theoretical* predictions, i.e. the ability to predict a given property using different theoretical/empirical frameworks but a single, common artificial neural network. The network predicts, given melt composition, the different parameters of the different theoretical/empirical equations, which, in turn, provide different values of the desired property. This allows one to predict melt viscosity using, for instance, the Adam-Gibbs or Free Volume equations depending on preference, and to compare final predictions as well as observe the connection and correlation between the different variables of the equations.

2.5.2. Trans-theoretical predictions

Various theories have been proposed to explain and reproduce the variations of the viscosity of liquids with parameters such as temperature, pressure or composition. For instance, the Adam-Gibbs theory (Adam and Gibbs, 1965) has been particularly successful in reproducing

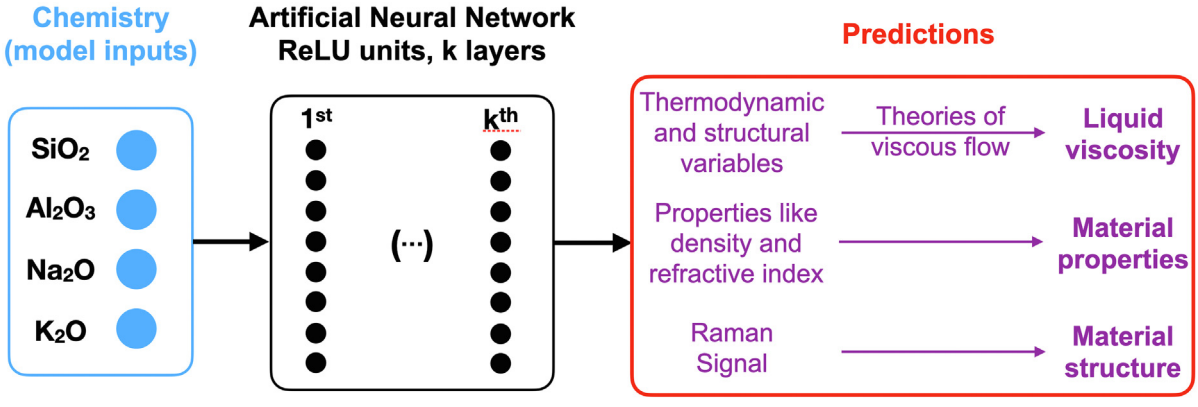

Fig. 2. Schematic of i-Melt. An artificial neural network takes input melt composition, and outputs various melt and glass properties. Once trained, relationships between chemistry, structure and properties of melts and glasses can be systematically explored.

relaxation and viscosity data of silicate melts (Richet, 1984; Scherer, 1984; Neuville and Richet, 1991; Bottinga et al., 1995; Bottinga and Richet, 1996). It assumes that liquid movements occur through cooperative molecular re-arrangements; viscosity (η) can be expressed as a function of temperature (T) and composition (x) via

$$log_{10}\eta(T,x) = A_e(x) + \frac{B_e(x)}{T\left(S^{conf}\left(T_g,x\right) + \int_{T_g}^{T} C_p^{conf}(x)/TdT\right)}, \quad (1)$$

with A_e representing a high-temperature limit, B_e a term proportional to the energy barriers opposed to molecular re-arrangements, and S^{conf} and C_p^{conf} the melt configurational entropy and heat capacity, respectively. $C_p^{conf}(T_g)$ is calculated from the difference $C_p^{liquid}(T_g) - C_p^{glass}(T_g)$; here, $C_p^{liquid}(T_g)$ was calculated from the model of Richet and Bottinga (1985) and $C_p^{glass}(T_g)$ is calculated from the Dulong-Petit limit of 3R, with R the perfect gas constant. T_g is the glass transition temperature. Here, we adopt the empirical definition of T_g as equal to the temperature for which $\eta = 10^{12}$ Pa·s, and the associated melt relaxation time is of $\sim$ 100 s. The T_g calculated from this definition agrees within 20–30 K with the T_g determined from calorimetric measurements (e.g., Russell and Giordano, 2017), which themselves depend on the cooling/heating rates during calorimetric measurements. The adopted T_g definition is thus coherent for viscosity modeling, as T_g derived from the viscosity data refers to the relaxed melt and its equilibrium structure.

Alternatively, one might adopt the Free Volume theory (Cohen and Grest, 1979, 1984), which states that melts present liquid-like and solid-like molecular cells, their mobility being ensured by atomic diffusivity within/between liquid-like cells. This takes the form

$$log_{10}\eta(T,x) = A_{FV}(x) + 2B_{FV}(x)/\left(T - T_{FV}(x) + \sqrt{\left((T - T_{FV}(x))^2 + C_{FV}(x)T\right)}\right), \quad (2)$$

with $A_{FV}(x)$ again representing the high-temperature limit, $B_{FV}(x)$ a constant that depends on the molecular volume, $C_{FV}(x)$ a constant that has a dimension of temperature and that should be positive, and $T_{FV}(x)$ a constant identified as the temperature at which continuity of liquid-like cells is reached.

Beyond the Free Volume and Adam-Gibbs models, many other theories have been proposed to describe the viscous flow of liquids. Among those, some are empirical like the Vogel-Fulcher-Tamman (VFT) equation:

$$log_{10}\eta(T,x) = A_{VFT}(x) + B_{VFT}(x)/(T - T_{VFT}(x)), \quad (3)$$

with A_{VFT}, B_{VFT} and T_{VFT} adjustable parameters. Others are based on different physical theories like the Avramov and Milchev (1988) (AM) model, or derive from the Adam-Gibbs theory like the MYEGA model (Mauro et al., 2009). Both propose equations relating viscosity, temperature as well as $T_g(x)$ and $m(x)$, the glass transition temperature and the fragility (equal to the gradient of the $\log_{10}$ viscosity *versus* inverse temperature curve at T_g) of a melt with composition x. The AM model is expressed as (Avramov, 2011):

$$log_{10}\eta(T,x) = A_{AM}(x) + (12 - A_{AM}(x))\left(T_g(x)/T\right)^{m(x)/(12-A_{AM}(x))} \quad (4)$$

with A_{AM} a pre-exponential terms proportional to $log_{10}\eta(T \to \infty)$. Similarly, the MYEGA equation takes the form:

$$log_{10}\eta(T,x) = A_e(x) + (12 - A_e(x))\left(T_g(x)/T\right)e^{(m(x)/(12-A_e(x))-1)\left(\frac{T_g(x)}{T}-1\right)} \quad (5)$$

with A_e a pre-exponential term proportional to $log_{10}\eta(T \to \infty)$ that was taken as equal to that in the Adam-Gibbs theory (Eq. (1)) because the MYEGA equation is a daughter product of the Adam-Gibbs theory. In practice, all the above equations model the viscosity dependence on temperature of silicate melts very well.

While the equations presented above are popular for silicate melts, no over-riding consensus exists towards any one model appropriate for all liquids. In fact, some of those models rely on very different theoretical backgrounds. The i-Melt approach circumvents the problem of choosing one particular theory by proposing a *trans-theoretical* approach. The artificial neural network is trained to predict melt viscosity using all five theoretical/empirical frameworks (Eqs. (1)–(5)). It provides optimal common values for parameters that appear in multiple theories, such as the glass transition temperature T_g. As a result, it allows comparison of viscosity predictions between the different theories, and observation of how parameters from the different theories correlate with each other, potentially providing insight into physical inter-relationships.

2.5.3. Data preparation: Train-Validation-Testing split and standardisation

If a model performs well when tested against the training dataset, but fails at making reliable predictions on new, unseen datasets, it is said to be 'overfitting'. This is a common problem affecting machine learning models. Here, we deploy several strategies to mitigate it. First, we monitor the phenomenon: the available datasets were split into three different, randomly chosen *training*, *validation* and *testing* subsets using the chemical_splitting *rampy* package function (Le Losq, 2018; Le Losq et al., 2019a) that relies on the scikit-learn (Pedregosa et al., 2011) train_test_split() algorithm. The data were randomly separated by composition to avoid the pitfall of having the same glass/melt composition in the different *training*, *validation* and *testing* subsets, a phenomenon known as 'data leakage' (Kaufman et al., 2012). As we wanted a significant amount of data in the testing subset for viscosity (because this is the most difficult property to predict here), $D_{viscosity}$ was separated with 20% of the compositions in the *testing* subset, 15% in the *validation* subset, and 65% in the *training* subset. $D_{optical}$ and $D_{density}$ were separated with 70% of the compositions in training, 15% in validation and 15% in testing.

D_{Raman} was divided in only two *train* and *validation* subsets due to its small size, with a 85–15 ratio. This is not problematic, because we do not aim at precise predictions of Raman spectra but rather use this dataset as a way to improve the general predictive capacity of the trained neural network through multitask learning.

During the training process, the *training* subset was used for training the model while the *validation* subset was used for monitoring overfit and to trigger early stopping. The latter method consists in stopping the training process when the Root-Mean-Square-Error (RMSE), measured between predictions and observations, on the validation data subset stops decreasing and starts diverging from that measured using the training data subset. This allows stopping the training process before the over-fitting phenomenon appears (Goodfellow et al., 2016). The final predictive abilities of the trained neural networks were then evaluated using the entirely unseen *testing* data subset.

After train-validation-test splitting, an important step in any machine learning data preprocessing is standardization of the data. In practice, appropriate data scaling is often essential to obtaining good convergence within algorithms (Goodfellow et al., 2016). The goal of re-scaling is to promote feature variations near unity and to ensure that all features have comparable numerical ranges: failure to do so tends to lead to instabilities in the gradient back-propagation process that is central to training neural networks. In the present study, we have implemented a custom approach. All chemical compositions inputs are in mole fractions, which (by definition) take values between 0 and 1. Therefore, these inputs do not require rescaling. The intensity of the Raman spectra were normalised to lie in the range 0 and 1: taking the Raman spectrum of a given composition, its intensities I were normalised according to the equation $(I\text{-}\min(I))/(\max(I)\text{-}\min(I))$. Other outputs such as viscosity, density and refractive index were not scaled, as scaling the outputs was not found to affect network convergence. However, with unscaled outputs, it is essential to initialise the bias of the output layer of the neural network to match the expected numerical range of the predictions to be made, as developed for (e.g.) Mixture Density Networks (Bishop, 2006). After pre-processing, the different scaled *training*, *validation* and *testing* data subsets were saved in Hierarchical Data Format HDF5 files for their future use.

2.5.4. i-Melt model technical implementation

i-Melt is implemented in the Python programming language, using the Pytorch machine learning library (Paszke et al., 2019). It takes four inputs: the mole fractions of the SiO_2, Al_2O_3, Na_2O and K_2O components. These are fed into to a neural network composed of k hidden layers, each one having a given number of activation units (a.k.a. neurons). Here, we chose to keep the same number of activation units in the different hidden layers. Alternative network structures (e.g. a "triangular" architecture with progressively fewer activation units in the deeper hidden layers) were explored, but did not markedly alter results. Following testing of various alternatives, we adopted the now-popular rectifier linear unit, ReLU (Glorot et al., 2011), as the activation function of activation units, so that an activation unit receiving input, x, returns output $y = \max(0,x)$. The outputs of the hidden layers were finally fed into two output linear layers. The first output layer returns vectors that are Raman spectra, calculated from the linear sum of the last neural network hidden layer. The second output linear layer returns 17 different values:

- the parameters A_e, A_{AM}, A_{FV} and A_{VFT} (Eqs. (1) to (5)), as well as the coefficients B_1 to B_3 and C_1 to C_3 of the Sellmeier equation (see Eq. (6) below) for the calculation of the glass refractive index n, are directly given by the linear outputs; and
- the parameters $S^{conf}(T_g)$, C_{FV}, T_g, T_{FV}, T_{VFT}, the melt fragility m, and the glass density d are given by the exponential of the outputs of the linear layer.

The use of the exponential function in the latter case was inspired by a similar strategy proposed by Bishop (2006) for Mixture Density Networks. It ensures that quantities are assigned positive values in accordance with their physical meaning. We also found the use of this strategy to aid rapid convergence during training. Indeed, we tested affecting the final output layer by relu() or sigmoid() activation functions, which also output only positive values, but this resulted in a much slower training; convergence was actually not achieved in most cases. B_e, B_{FV} *and* B_{VFT} were calculated from Eqs. (1) and (5) and the knowledge of the other parameters; for instance, $B_e = (12 - A_e)/(T_g\ S^{conf}(T_g))$, with A_e, T_g and $S^{conf}(T_g)$ values given by the neural network. The coefficients B_1 to B_3 and C_1 to C_3 are used to predict the refractive index at given wavelength, $n(\lambda)$, via the Sellmeier equation:

$$n(\lambda) = \sqrt{\left(1 + \frac{B_1 \times \lambda^2}{\lambda^2 - C_1} + \frac{B_2 \times \lambda^2}{\lambda^2 - C_2} + \frac{B_3 \times \lambda^2}{\lambda^2 - C_3}\right)}. \quad (6)$$

The artificial neural network allows us, therefore, to input chemical compositions and to obtain predictions for:

- melt viscosity, within five distinct theoretical or empirical frameworks,
- glass transition temperature,
- latent variables like configurational entropy and fragility,
- glass density,
- glass refractive index as a function of wavelength, and
- glass Raman spectra.

These predictions depend on a large number of tuneable parameters integral to the neural network. During network training, these parameters are optimized, seeking values that enable good average predictive performance when applied to examples in our database of observed glass properties.

2.5.5. Training i-Melt

During training, we monitored the root-mean square errors (RMSE) between measurements and predictions for viscosity from Eqs. (1) to (5) as well as density, optical

refractive index and Raman spectra, on the training and validation data subsets. A loss function was also added for known $S^{conf}(T_g)$ values from the dataset $D_{viscosity}$. This was necessary because $S^{conf}(T_g)$ is a parameter that is difficult to evaluate because of its strong correlation with B_e. This correlation prevents Eq. (1) from having a non-ambiguous solution. In practice, the neural network can predict a nearly constant value for the first and large variations for the second, and still obtain good predictive results for viscosity. Addition of a loss function for known $S^{conf}(T_g)$ solved this problem. The total loss L_{total} was computed from the sum of the different loss functions L_i, $L_{total} = \sum w_i L_i$, affected by scaling factors w_i that were adjusted manually such that each loss was around unity after training. Back-propagation was performed using the automatic differentiation methods implemented in Pytorch.

Batch training was performed using the Adam optimizer with a learning rate of 0.0006 (manually tuned), and monitoring the global loss on the *training* and *validation* data subsets. Early stopping, which consists in stopping the training process when the first signs of over-fitting are detected (Goodfellow et al., 2016), was used to avoid overfitting: when the global loss function on the *validation* data subset ceased to decrease for more than a given number of epochs (manually tuned), training was halted and the network exhibiting the best validation loss was saved. Dropout (Srivastava et al., 2014), a method that entails randomly turning off a given fraction of activation units at each training iteration, was also tested. This method is known to promote generalization and reduce overfitting.

2.5.6. Optimization of the artificial neural network architecture

Before presenting any results regarding the performance of the model, we first document the optimal architecture and the way we searched for it. This optimal architecture is important as it determines its performance to fit the existing data, its sensitivity to overfitting, and its generalization ability (i.e. its ability to provide precise and accurate predictions for new, unseen compositions). Several methods allow searching for the optimal neural network architecture, like random search (Bergstra and Bengio, 2012) or Bayesian optimization (Snoek et al., 2012). In this study, the architecture of the hidden layers was optimized via a random search process (Bergstra and Bengio, 2012). With sufficient iterations, such random search allows sampling the model space with a good precision.

Two numerical experiments were performed. The first explored how the neural network architecture affected its performance. For this experiment, we randomly varied the number of hidden layers from 1 to 6, that of hidden activation units from 10 to 500 and the dropout parameter *p from 0 to 0.5*. 3000 neural networks with different architectures were generated using the random number generator from the python library *numpy*. The results of this test show that a moderately deep neural network with 3 to 5 layers and 200–300 units per layer provide the best results, with limited overfitting (Supplementary Fig. 1). Those results indicate that moderately deep neural network generalizes better than shallow ones on this problem with small datasets. The dropout method helps slightly in preventing overfitting, but is not a critical feature in the present case (Supplementary Fig. 1). Following this test, we selected a reference architecture with 4 layers, 300 neurons per layer, and a dropout of 0.01.

The second test investigated the effect of the number of training compositions in the training dataset on the overall performance of the model, using the reference architecture selected following the random training phase (see above). Deep neural networks are generally known to be "data-eager", requiring large datasets for efficient training. To identify the point at which we can start trusting the results of i-MELT, we generated new training datasets for $D_{viscosity}$ with different numbers of compositions, from ~20 up to more than 120 (Supplementary Fig. 1). In practice, this represents many more data points, as there are multiple viscosity measurements for each composition (on average, ~10 observations per composition). For the system considered here, we find satisfactory performance once the dataset reaches around 70 distinct compositions. With more than ~70 compositions in the training dataset, RMSE values between model predictions and measurements become lower than 0.6 $\log_{10}$ Pa·s. Furthermore, the training and validation subsets exhibit similar RMSE values, indicating that any overfitting problem is limited (Supplementary Fig. 1). With the chosen data splitting (see above), we have 113 different compositions in training $D_{viscosity}$ (over a total of 173), and 160 (over a total of 223) and 139 individual compositions (total 205) in the training $D_{optical}$ and $D_{density}$, respectively. The datasets are thus large enough for training efficiently the networks. The only limit is for Raman spectra, with training D_{Raman} having only 48 compositions (total 58). As already explicitly presented, we thus do not expect high performance for Raman spectra predictions.

To make the final predictions and further limit the overfitting problems, we trained 100 candidate neural networks with the reference architecture, and selected the 10 best ones. All reported predictions by i-Melt are calculated from the average of those from the 10 best neural networks, following the bagging method (Breiman, 1996) that promotes generalization (good predictions on new samples) of machine learning algorithms. This further allows us to provide error bars and error envelopes, which can be calculated from the standard deviation of the predictions of the 10 neural networks. The use of the bagging method, combined with the developed training protocol, allowed i-Melt to provide good generalization abilities. Furthermore, multi-task learning is performed here, as the neural network is trained to predict different features (properties like density or T_g, observables like Raman spectra…) from the same objects. This helped further limiting overfitting because artificial neural networks learning to predict multiple related features/observables tend to show better prediction abilities compared to those trained to predict only a given task/parameter/feature (Caruana, 1997). We observed this by performing a few tests, training a few neural networks to only predict viscosity. Those resulted in RMSE of ~0.5–0.6 $\log_{10}$ Pa·s, higher than those of neural networks trained to predict multiple properties (equal to or lower than 0.4 $\log_{10}$ Pa·s, see below).

3. RESULTS

3.1. Melt and glass property predictions

Using the unseen samples from the testing data subsets, it is possible to test whether i-Melt can provide good predictions despite limited experimental datasets. Trans-theoretical predictions of η (Fig. 3, see also Supplementary Fig. 2) are possible with good precision. The RMSE values are equal to 0.4 $\log_{10}$ Pa·s on the testing data subset (Table 3). For comparison, the RMSE of the best empirical magma viscosity models typically are higher than, or equal to 0.6 $\log_{10}$ Pa·s (e.g. Giordano et al., 2008). Eqs. (1) to (5) all yield similar values (Supplementary Fig. 2, Table 3). In detail, predictions in the supercooled temperature domain are affected by larger errors than predictions in the sub-liquidus to super-liquidus domain: testing RMSE values (all equations considered) are in the range 0.5–0.7 $\log_{10}$ Pa·s when considering only data in the 10^7–10^{15} Pa·s range, whereas they are in the range 0.2–0.3 $\log_{10}$ Pa·s for data below 10^7 Pa·s.

The melt/glass properties are also well predicted by i-Melt. Known viscous T_g and $S^{conf}(T_g)$ are predicted within 19 K and 0.8 J mol^{-1} K^{-1}, respectively (Table 3, Supplementary Fig. 3). The glass density and refractive index are predicted to within 0.02 g cm^{-3} and 0.006, respectively (Table 3). For the two latter properties, a few outliers are visible and correspond to extreme compositions along the SiO_2-Al_2O_3 join (Fig. 1c, d , Supplementary Fig. 3) for which only a few data points are available. This is therefore unsurprising, particularly considering that there are large variations in glass and melt properties along this join (e.g., Okuno et al., 2005; Ando et al., 2018).

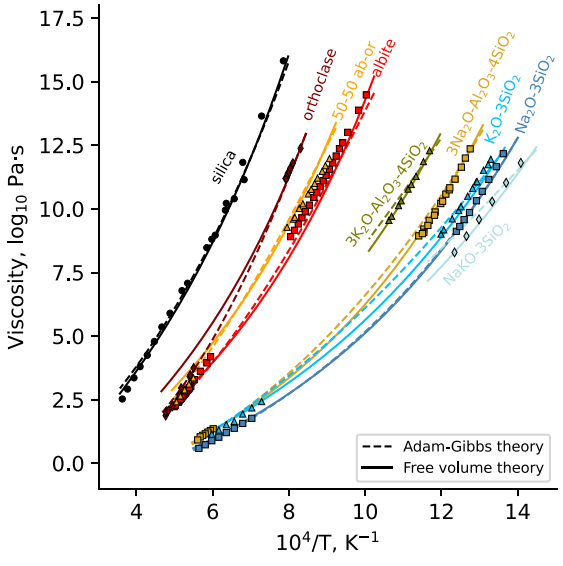

Fig. 3. Prediction examples of melt viscosity. Viscosity can be predicted using various theories with a great accuracy, as shown by examples highlighting the good match between measurements (symbols) and model (curves) predictions from the Adam-Gibbs and Free Volume theories.

3.2. Structural information through Raman spectra predictions

In addition to physical and thermodynamic properties, i-Melt has the ability to predict structure-dependent features such as Raman spectra of glass. Considering the very small experimental Raman dataset (Fig. 1b), global variations of Raman signals have been well-captured. The 400–1250 cm^{-1} portion of the glass Raman spectra can be predicted within a relative error of ~25% (average relative RMSE between observed and predicted spectra from the validation data subset). For instance, Fig. 4a shows examples of the prediction of the Raman spectra of glasses along the Na_2O-SiO_2 binary join.

Structural information can be extracted from i-Melt Raman spectra predictions. Fig. 4b shows, for instance, the large decrease in the signals assigned to bending/stretching of Q^n-Q^n intertetrahedral vibrations in the glass network (Bell et al., 1968; Sen and Thorpe, 1977; Furukawa et al., 1981; McMillan, 1984) with addition of Na_2O in SiO_2. These variations are accompanied by increasing intensity near 1100 cm^{-1}, a signal that results from Si—O stretching in Q^3 units (Brawer and White, 1975, 1977; Furukawa et al., 1981; Mysen et al., 1982a; McMillan, 1984). When the Na_2O fraction is above 0.3, we further see the increase of the intensity of a signal near 950 cm^{-1} that can be assigned to Si—O stretching in Q^2 units (Brawer and White, 1975, 1977; Furukawa et al., 1981; Mysen et al., 1982a; McMillan, 1984).

The analysis of predicted signals, such as those showed in Fig. 4b, through peak fitting or decomposition methods (e.g., see Mysen et al., 1982a; Herzog and Zakaznova-Herzog, 2011) can allow extracting further structural information about the glass. At the moment, for the sake of simplicity, we focus on extracting a simple parameter: R_{Raman}, the ratio of intra- and inter-tetrahedral aluminosilicate vibrations. R_{Raman} is the ratio between A_{LW}, the integrated intensity in the 0–670 cm^{-1} range, and A_{HW}, the integrated intensity in the 800–1300 cm^{-1} range:

$$R_{Raman} = \frac{A_{LW}}{A_{HW}}. \quad (7)$$

A_{LW} integrates the signals assigned to bending/stretching of Q^n-Q^n intertetrahedral vibrations in the glass network (Bell et al., 1968; Sen and Thorpe, 1977; Furukawa et al., 1981; McMillan, 1984), and A_{HW} those assigned to stretching of Al—O and Si—O bonds in Q^n units (Brawer and White, 1975, 1977; Virgo et al., 1980; Furukawa et al., 1981; Mysen et al., 1982a,b; McMillan, 1984). The integration boundaries were selected by observing all the spectra plotted together. They correspond to common Raman shifts that delimit the frequencies of the inter-tetrahedral Q^n – Q^n and intra-tetrahedral Q^n vibrational regions. While some small changes could be made in some cases, our selection of common boundaries for all glass Raman spectra robustly captures the general trend.

R_{Raman} is a simple but interesting parameter, because it appears to correlate with structural parameters like NBO/T (number of non-bridging oxygens per tetrahedral unit, see Mysen et al., 1982b), and, as such, it was used to pro-

Table 3
Root-mean-square errors (RMSE) between predictions and measurements.

Data subset	Training	Validation	Testing
Adam-Gibbs (Eq. (1), $\log_{10}$ Pa·s)	0.3	0.3	0.4
Free Volume (Eq. (2), $\log_{10}$ Pa·s)	0.3	0.4	0.4
VFT (Eq. (3), $\log_{10}$ Pa·s)	0.3	0.4	0.4
MYEGA (Eq. (5), $\log_{10}$ Pa·s)	0.3	0.4	0.4
Avramov-Milchev (Eq. (4), $\log_{10}$ Pa·s)	0.3	0.4	0.4
Density (g cm^{-1})	0.01	0.02	0.01
Raman spectra (%, relative RMSE)	20	25	-
Refractive index	0.003	0.004	0.006

pose viscosity models based on the Raman spectra of glasses (Giordano and Russell, 2018). i-Melt can predict R_{Raman} within an error of ±0.5, such that we can use the model to obtain first-order information about R_{Raman} variations and glass structure. For instance, along the Na_2O-SiO_2 binary, we observe that the addition of network modifier Na_2O to silica is accompanied by a strong decrease in R_{Raman} that originates from the increase in the glass NBO/T (Fig. 5a). This observation thus corroborates the findings of Giordano and Russell (2018). R_{Raman} thus can serve as a measure of the glass SiO_2-AlO_2 network connectivity (i.e. formation of T-O-T bonds, with T = Si, Al): the higher R_{raman} is, the higher the aluminosilicate network connectivity, the lower the NBO/T. Because of such link, R_{Raman} may be linked to variations in melt properties, as suggested by the study of Giordano and Russell (2018). However, looking at sodium tectosilicate glasses with Al/Na = 1 (Fig. 5b), R_{Raman} is also influenced by other effects. Indeed, it decreases with decreasing the silica content in fully polymerized tectosilicate melts. This reflects the evolution of

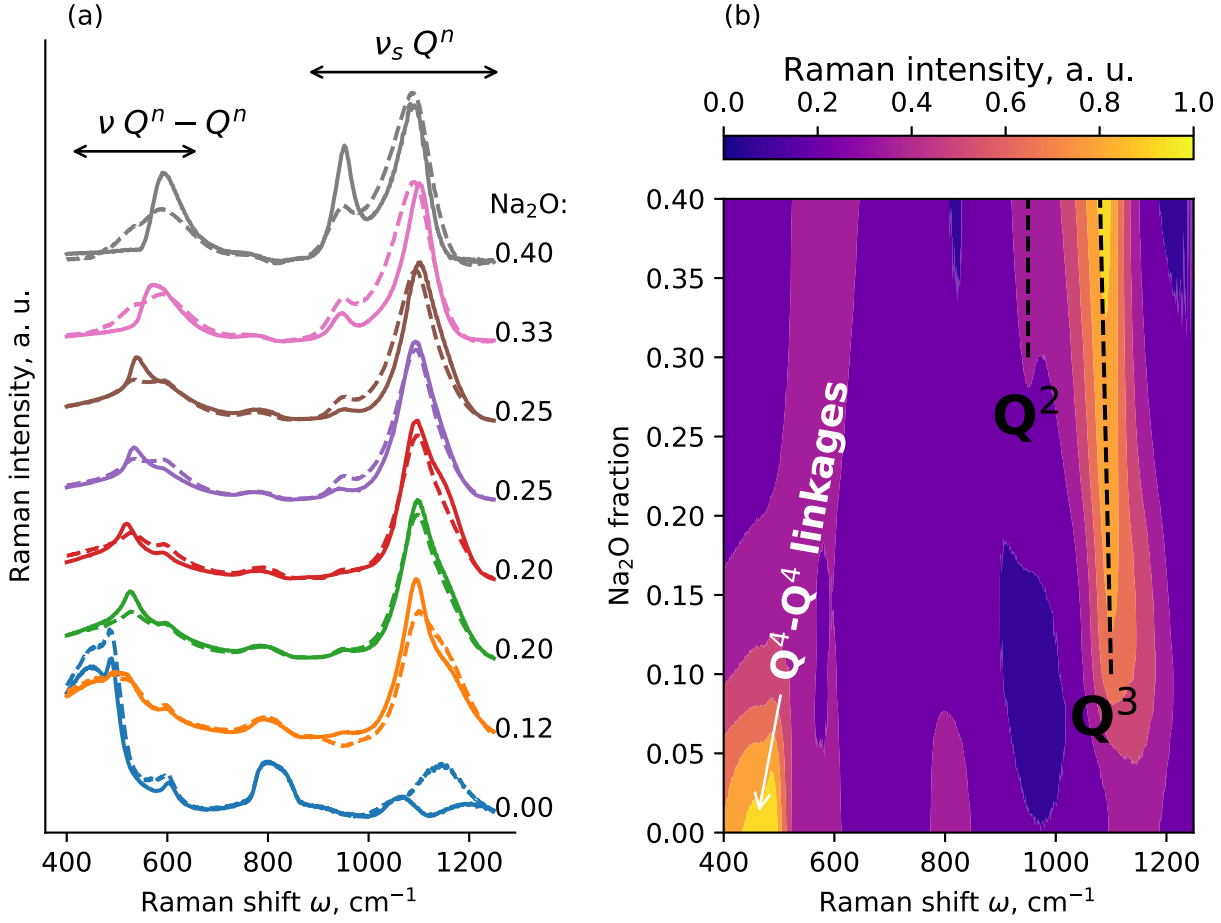

Fig. 4. Glass Raman spectra along the SiO_2-Na_2O binary. (a) Comparison between experimental (plain lines) and predicted (dashed lines). Ranges of Si-O-Si intertetrahedral (Q^n-Q^n) vibrations and Si—O stretching vibrations in Q^n units are indicated at the top. (b) 2D contour plot of the predicted Raman intensities (a. u.) as a function of Raman shifts (cm^{-1}) and Na_2O content (mol fraction).

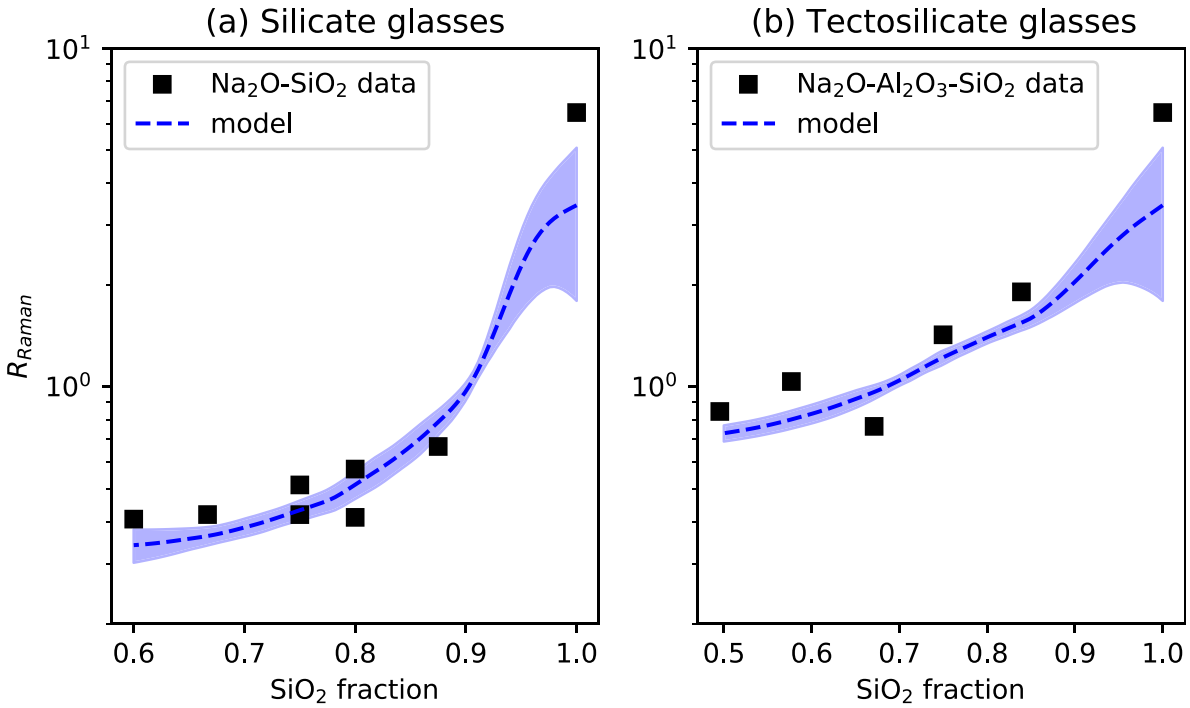

Fig. 5. R_{Raman} parameter (a. u., see text) as a function of silica mol fraction in (a) silicate Na_2O-SiO_2 and (b) tectosilicate $NaAlO_4$-SiO_2 glasses. Symbols are data, dashed lines are model predictions (mean of predictions from 10 models), and the blue shaded area show the 2σ confidence intervals (standard deviations of predictions from 10 models).

Raman spectra as Al substitutes Si along the SiO_2-$NaAlO_4$ join, which results from structural variations such as decreasing intertetrahedral bond angles (Seifert et al., 1982; Neuville and Mysen, 1996).

There is a substantial data gap for R_{raman} between ~2 and ~4 (the value corresponding to that of silica glass) because there are very few Raman spectra in the dataset at SiO_2 concentrations above ~90 mol%, and R_{raman} varies strongly with silica content at this level. This data gap originates from the difficulty to obtaining samples above ~90 mol% SiO_2, and only one spectrum (that of silica) constrains the model at very high R_{Raman} values.. At such high silica concentrations, unmixing can happen during quench for Na_2O-SiO_2 compositions (e.g., Jarry and Richet, 2001). In addition, high liquidus temperatures make the synthesis of glasses difficult for Al-bearing compositions (Schairer and Bowen, 1955, 1956). Nevertheless, information from new experiments in silica-rich melts could be important to bring information to the model about melt/glass structural behavior between an extreme composition like SiO_2 and multicomponent melts/glasses.

3.3. Model internal consistency

The ability to predict the melt fragility, m, permits further testing of the internal consistency of i-Melt. Experimental data indicate that a direct correlation between m and the ratio of the configurational heat capacity at T_g over the configurational entropy at the glass transition, $C_p^{conf}(T_g)/S^{conf}(T_g)$, exists (Webb, 2008; Russell and Giordano, 2017). This is predicted by the Adam and Gibbs theory because (Toplis et al., 1997a):

$$m = \frac{B_e}{S^{conf}(T_g)T_g}\left[1 + \frac{C_p^{conf}(T_g)}{S^{conf}(T_g)}\right]. \quad (8)$$

We find that i-Melt also predicts this correlation (Fig. 6). The model predictions fall between the trends found by the experimental studies of Russell and Giordano (2017) and Webb (2008). The model is, thus, internally consistent. Some scatter is visible in Fig. 6. It most probably arises from the propagation of the uncertainties affecting the different predicted values (i.e., m and $S^{conf}(T_g)$) as well as the melt and glass C_p calculations. The combination and propagation of all those sources of uncertainties probably explains the greater scatter observed in Fig. 6 compared to experimental studies (Webb, 2008; Russell and Giordano, 2017). Finally, some outliers are also visible, and correspond to compositions mostly on the SiO_2-Al_2O_3 join. Along this binary, no supercooled viscosity data are available to constrain the melt fragility, and melt/glass C_p predictions probably are affected by important errors. The combination of those two problems probably explains the occurrence of the observed outliers.

3.4. Systematic predictions in the Na_2O-Al_2O_3-SiO_2 and K_2O-Al_2O_3-SiO_2 systems

The Na_2O-K_2O-Al_2O_3-SiO_2 system is of paramount importance for alkali magmatic melts, particularly rhyolites

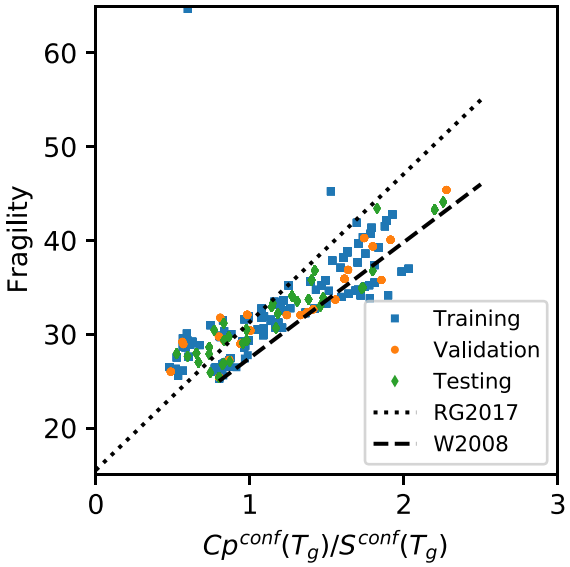

Fig. 6. Glass fragility *versus* melt $C_p^{conf}(T_g)/S^{conf}(T_g)$ ratio. Symbols are predictions of the deep learning framework on the different subsets of the $D_{viscosity}$ dataset (mean of predictions from 10 models). The dashed line is the relationship observed by Webb (2008, abbreviated W2008 in the figure) using experimental heat capacity data, and the dotted line is that observed by Russell and Giordano (2017, abbreviated RG2017 in the figure). Except two extreme outliers that corresponds to Al_2O_3-SiO_2 melts with more than 30 mol% Al_2O_3, a general good agreement is observed.

and granites. With i-Melt, we can go a step further and observe how several properties vary with composition in this system. For the sake of clarity, we focus here on showing variations in the ternary Na_2O-Al_2O_3-SiO_2 and K_2O-Al_2O_3-SiO_2 systems. To calculate properties, we first generated 10,000 random compositions in the ternary Na_2O-Al_2O_3-SiO_2 and K_2O-Al_2O_3-SiO_2 systems, from 50 mol% SiO_2 to 100 mol% SiO_2, and asked i-Melt to predict several glass and melt properties.

3.4.1. Glass properties

i-Melt allows systematic exploration of the variations of the viscous glass transition temperature with melt composition (Fig. 7a, b). In the Na_2O-Al_2O_3-SiO_2 and K_2O-Al_2O_3-SiO_2 systems, the model predicts the well known decrease of T_g with addition of alkali metals, and increase with addition of SiO_2, and, to a lesser extent, Al_2O_3 (Fig. 7a, b). In the potassic aluminosilicate system, there is a local T_g maximum near the $KAlSi_2O_6$ composition on the SiO_2-KAl_2O_4 binary, at ~66 mol% SiO_2 (Fig. 7b). This maximum correlates with a maximum in liquidus temperatures ($T_{liquidus}$). That of leucite $KAlSi_2O_6$ is of 1693 °C (Schairer and Bowen, 1955). It corresponds to a local maximum along the SiO_2-KAl_2O_4 binary that correlates with the T_g maximum observed in Fig. 7b. No such maximum in T_g is observed on the sodic SiO_2-$NaAl_2O_4$ binary, in agreement with the absence of a $T_{liquidus}$ maximum along this binary (Schairer and Bowen, 1956). This agrees with the general correlation between T_g and $T_{liquidus}$ (e.g., see Sakka and MacKenzie, 1971 and references therein), leading us to suggest that a model such as i-Melt could also predict $T_{liquidus}$.

Compared to T_g, glass density or optical refractive index display simpler variations with glass composition (Fig. 7c–f). As it is well known, glass density mostly depends on the concentrations of Na_2O and Al_2O_3 added to SiO_2. i-Melt reproduces this dependence well. The glass optical refractive index variations show a different pattern, the addition of Al_2O_3 having a greater effect than that of Na_2O at comparable molar contents. The optical refractive index actually does not correlate strongly with any of the thermodynamic/dynamic variables. This is expected because the optical refractive index is mostly controlled by the electronic properties of the atoms present in the glass. Interestingly, glass density correlates with fragility (Spearman correlation coefficient $r_s = 0.87$). Similar variations are thus visible when comparing melt fragility and glass density in the ternary sodium and potassium aluminosilicate diagrams (Figs. 7 and 8).

3.4.2. Melt fragility

Two of the selected viscosity equations (Eqs. (4) and (5)) share melt fragility as a common parameter in their expressions. Melt fragility is equal to the slope of the $\log_{10}$ of viscosity versus the inverse of temperature at T_g, and scales with the ratio between C_p^{conf} and S^{conf} at T_g (Eq. (8)). In the investigated system, melt fragility varies smoothly with the SiO_2 and Al_2O_3 concentrations (Fig. 8a, b). Increasing melt SiO_2 content leads to large decreases in melt fragility, an observation that agrees with previous ones in alkali (e.g., Toplis et al., 1997a) and even alkaline-earth (e.g., Bechgaard et al., 2017) aluminosilicate compositions. Changing the K/(K + Na) ratio does not lead to large changes in fragility (Fig. 8c–f), in agreement with the observations of Robert et al. (2019). At constant silica concentration, depolymerized alkali silicate melts are slightly more fragile than polymerized tectosilicate melts. i-Melt predicts that peraluminous Al-rich melts generally are more and more fragile with increasing Al concentration. However, at ratios of Al/(Al + Na + K) higher than ~0.6, the model is forced to extrapolate due to the lack of data (Fig. 1). This observation could indicate that (i) extrapolations are not fully robust and should be considered with care, or (ii) high Al concentrations indeed lead to high melt fragility.

3.4.3. Configurational entropy of alkali aluminosilicate melts

$S^{conf}(T_g)$ shows a complex dependence on melt composition and structure because it has two sources: (i) a topological origin that results from the network topology (distribution of bond angles, bond distances, etc.), and (ii) a chemical one that results from the mixing of cations in the atomic structure. The later source shows variations that can be complex. Indeed, mixing between two cations in silicate and aluminosilicate melts can be random (Neuville and Richet, 1991; Neuville and Mysen, 1996) or not (Seifert et al., 1982; Lee, 2005; Neuville, 2006; Le Losq and Neuville, 2013, 2017; Robert et al., 2019). It can occur between Si and Al "network formers" (Neuville and Mysen, 1996), between "network modifier" metal cations (Richet, 1984; Neuville and Richet, 1991; Lee et al., 2003) or

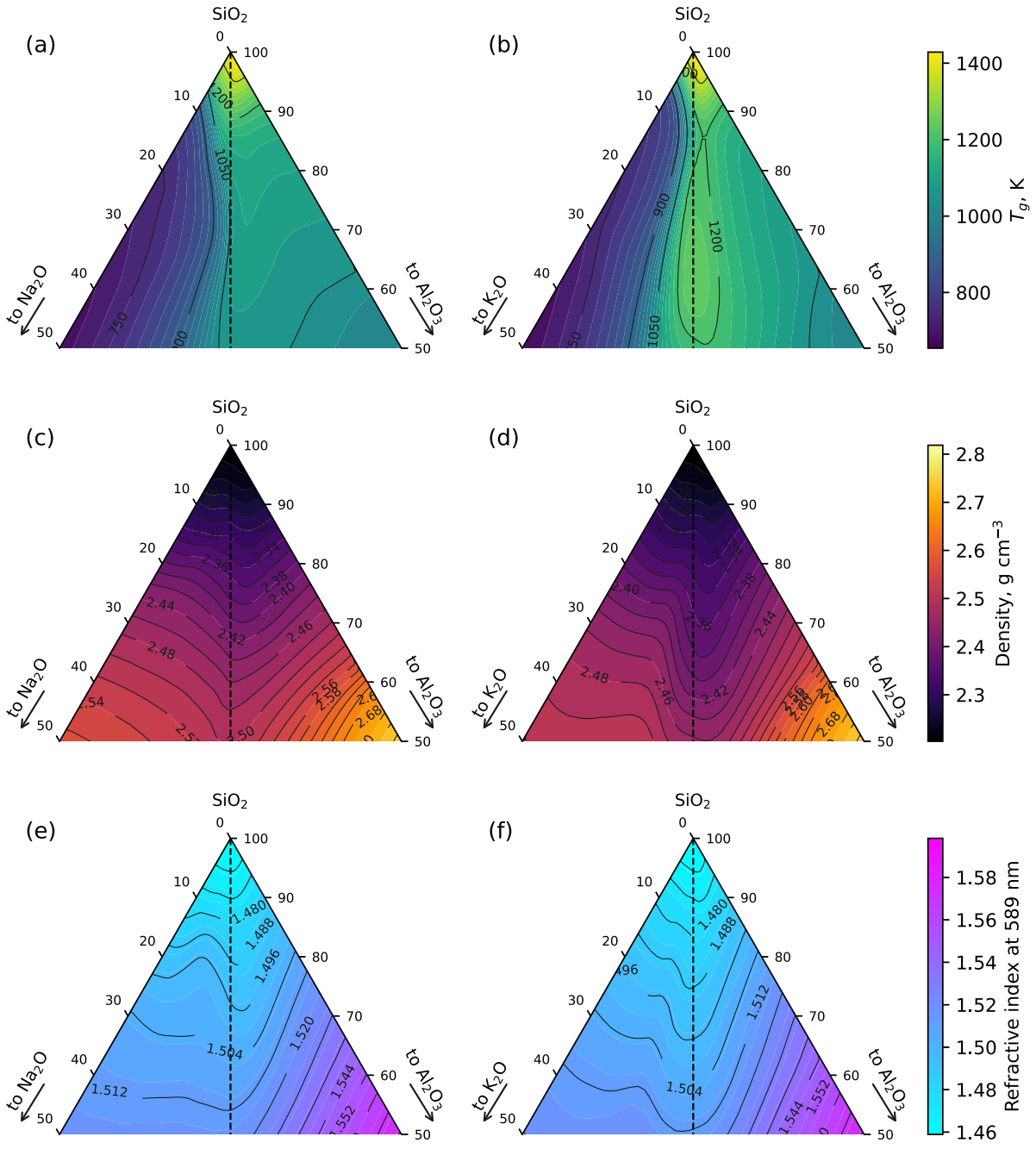

Fig. 7. Deep learning framework predicted variations in (a,b) glass transition temperature T_g, (c,d) relative density and (e,f) refractive index at 589 nm in the upper part (SiO_2 > 50 mol%) of the ternary Na (left) and K (right) aluminosilicate systems.

between the "charge compensator" metal cations that compensate the electrical charge deficit of AlO_4^- units in aluminosilicate compositions (e.g., Neuville and Richet, 1991; Robert et al., 2019). Such mixing effects usually are difficult to predict, and subject to interpretation.

i-Melt helps solve this problem by enabling systematic quantification and visualization of such phenomena. As observed in Fig. 9, $S^{conf}(T_g)$ displays systematic variations as a function of the chemical composition of alkali aluminosilicate melts. Increasing Al concentration leads to decreasing $S^{conf}(T_g)$ (Fig. 9a,b). The Al/(Na + K) ratio also largely affects the way Na and K mix. Without Al, their interaction results in an entropy excess (Fig. 9c) and, hence, in a decrease in melt viscosity because viscosity is proportional to the inverse of $S^{conf}(T_g)$ (Eq. (1)). This pattern changes with increasing Al/(Na + K), because as Al is introduced into the glass network, the role of alkali metals changes (see chapters 4 and 8 of Mysen and Richet, 2019). In the presence of Al, Na and K are present in different structural environments (McKeown et al., 1985; Jackson et al., 1987; Le Losq and Neuville, 2017), inducing less and less excess entropy of mixing as Al/(Na + K) increases

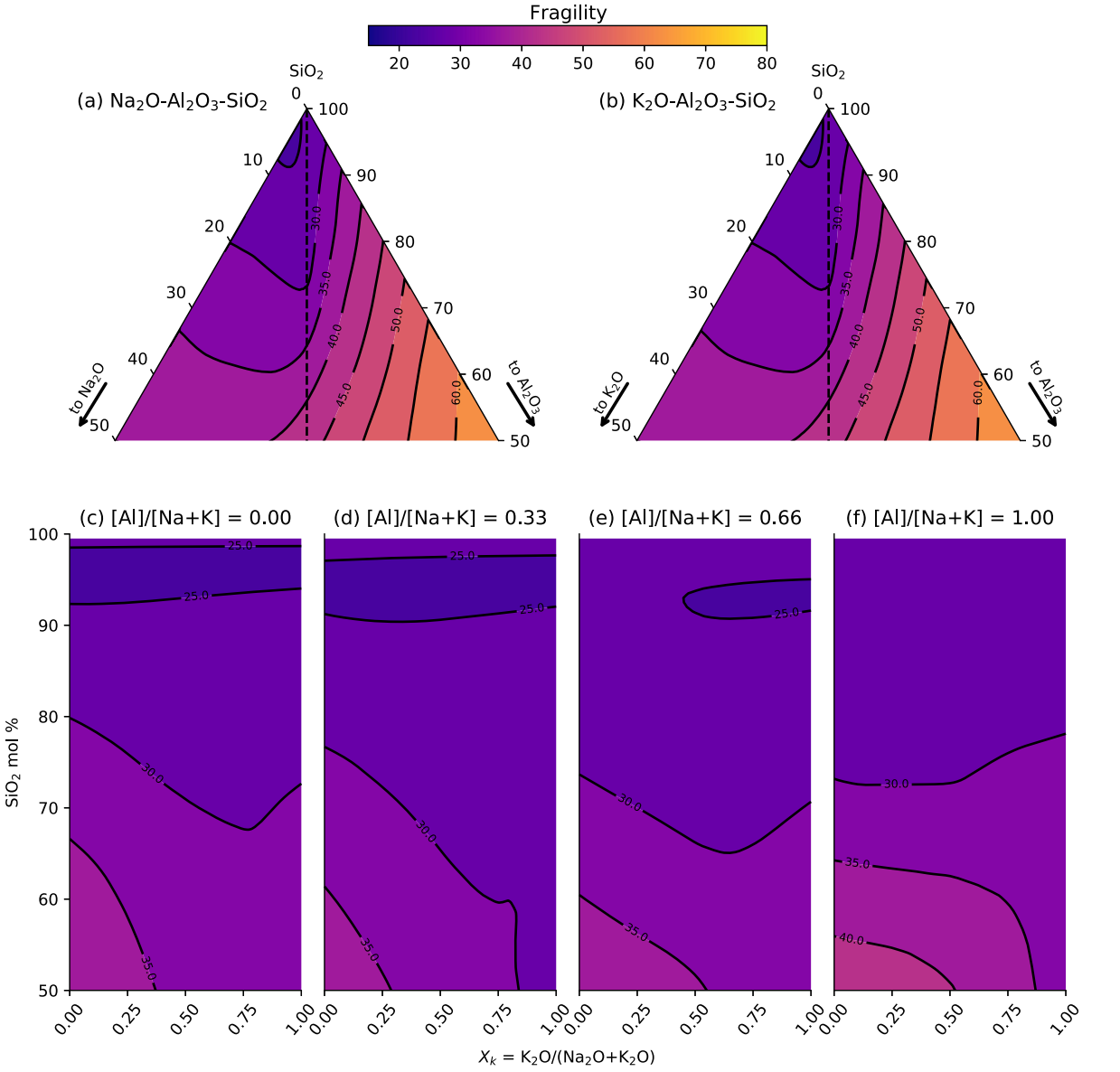

Fig. 8. Melt fragility, m, of melts in the upper part (SiO_2 > 50 mol%) of the K_2O-Na_2O-Al_2O_3-SiO_2 system. Fragility is represented in the upper part of the ternary sodium (a) and potassium (b) aluminosilicate systems, as well as as a function of the silica fraction and the potassium to total alkali ratio of silicate, peralkaline and tectosilicate melts (c, d, e, f).

(Le Losq et al., 2017; Robert et al., 2019). As a result, $S^{conf}(T_g)$ varies more and more linearly upon mixing Na and K in Al-rich melts (Fig. 9d–f). Finally, i-Melt predicts small $S^{conf}(T_g)$ values for K-rich and Al-rich melts (Fig. 9b, f), in agreement with experimental findings (Richet and Bottinga, 1984; Le Losq and Neuville, 2013; Le Losq et al., 2017; Robert et al., 2019). This is explained by Al and K respectively promoting the polymerization of the melt network (decrease in NBO/T) and the formation of larger cooperative molecular domains involved in the melt viscous flow (e.g., Riebling, 1966; Taylor and Rindone, 1970; Rammensee and Fraser, 1982; Mysen, 1988; Toplis et al., 1997b; Mysen and Toplis, 2007; Xiang et al., 2013; Le Losq et al., 2017). The variations in $S^{conf}(T_g)$ with the composition of aluminosilicate melts, thus, depend mostly on (i) how metal cations interact together, and (ii) on how those interactions are affected by the presence of Al, and by Si-Al interactions.

3.4.4. Extrapolations

As "intelligent" as they can be, machine learning algorithms still are interpolative in nature. Therefore, it is not necessarily wise to ask them to perform predictions outside the range of their training dataset. Here, we tested how the model generally behaves when performing such extrapolations by (i) removing some density and optical refractive index data along the SiO_2-Al_2O_3 join and (ii) trying to predict a value for a composition very far from those included

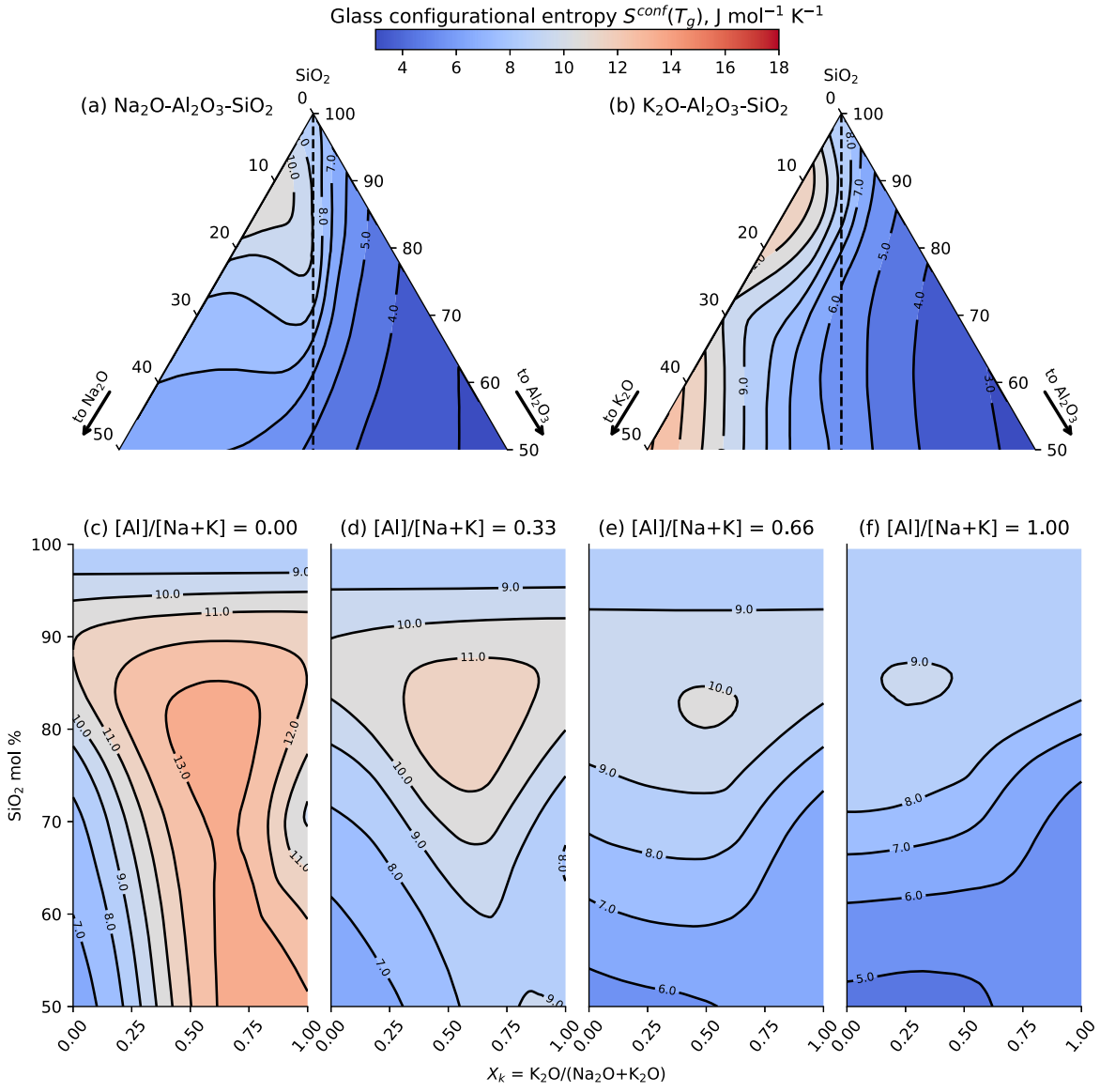

Fig. 9. Configurational entropy at T_g, $S^{conf}(T_g)$, of melts in the upper part ($SiO_2 > 50$ mol%) of the K_2O-Na_2O-Al_2O_3-SiO_2 system. $S^{conf}(T_g)$ vary non-linearly with oxide contents in the ternary diagrams (a) Na_2O-Al_2O_3-SiO_2 and (b) K_2O-Al_2O_3-SiO_2. In silicate melts (c), a mixed alkali effect (MAE) is observed upon Na-K mixing. It disappears as [Al]/[Na + K] increases (d, e, f).

in its training dataset, the T_g *of* Al_2O_3. Regarding (i), the model tends to provide a constant value for density or optical refractive index when asked to make predictions for compositions beyond those included in its training set. This situation is both good and bad. It is good because it indicates that the model does not "explode", i.e. starts to predict small or large values very different from the mean ones when extrapolating (this is what happens traditionally with polynomial functions, for instance). It obviously is bad because it means that i-Melt will remains mostly interpolative in nature for some parameters like fragility, at least for the moment. Turning to the second test, we first estimated the Al_2O_3 T_g from the data of Secrist et al. (1965) and Urbain et al. (1982). Secrist et al. (1965) estimated a viscosity of 4×10^{10} Pa·s at 1173 K from the rate of crystallization of vapor-formed Al_2O_3 amorphous films. Fitting the high temperature viscosity data of Urbain et al. (1982) for Al_2O_3 and this point with equation (3), we have for Al_2O_3 melt $A_{VFT} = -2.8 \pm 0.1$, $B_{VFT} = 1842 \pm 176$ and $C_{VFT} = 1035 \pm 19$, and $T_g = 1035 \pm 19$ K. i-Melt predicts a T_g of 815 ± 37 K for Al_2O_3. This T_g estimation is realistic (the model did not 'explode') but significantly below the value calculated from viscosity data. This highlights that extrapolations with models like i-Melt may produce apparently realistic results, but still may be far from the true value.

With limited data, it is inevitable that i-Melt has to extrapolate for some predictions. Following the above

discussion, caution is needed. Fortunately, for some properties, results appear to be broadly plausible. This is the case for $S^{conf}(T_g)$. For instance, the model predicts a continuous decrease of $S^{conf}(T_g)$ with increasing Al_2O_3 in the peraluminous field (Fig. 9a, b), a prediction that agrees with experimental data in sodium peraluminous melts (Le Losq et al., 2014). To conclude, this discussion highlights that, if necessary, machine learning model extrapolations can be performed but should be considered with care, making sure that predictions are realistic compared to the known trends of material properties.

4. DISCUSSION

Several questions motivated the development of i-Melt and its current focus on the Na_2O-K_2O-Al_2O_3-SiO_2 system:

- How are chemical composition, atomic structure and physical properties of such alkali aluminosilicate melts connected?
- How do changes in the Na/K ratio affect the structure and properties of alkali aluminosilicate melts? What role does this play in the eruptive dynamics of volcanic eruptions involving rhyolite magmas?

4.1. Exploration of composition-structure–property links

As i-Melt allows a systematic exploration of the links between different observed and latent variables, we can investigate the contributions of topological (i.e, the geometry and interconnectivity of the T-O-T network, with T = Si,Al) and chemical effects (i.e., effects resulting from mixing different cations in similar sites) to different properties. For example, R_{Raman}, and, therefore, the glass network topology correlates with the glass transition temperature (Fig. 10a). It also correlates with quantities proportional to energy barriers opposed to ionic mobility in melts like the B_{FV} term of the Free Volume viscosity equation (Fig. 10b, Eq. (2)). This result agrees very well with the general knowledge of the influence of the topology/connectivity of the aluminosilicate network on melt transport properties (e.g., Bockris et al., 1955; Mysen et al., 1980; Mysen, 1991).

However, the correlation between R_{Raman} and glass transition temperature T_g is not perfect. Some influence of the glass composition on the R_{Raman} *versus* T_g relationship is visible in Fig. 10a. It probably originates from metal cation chemical mixing effects that can affect T_g (Isard, 1969; Day, 1976). Indeed, while cationic mixing effects only slightly influence properties directly linked to the aluminosilicate network connectivity (Le Losq and Neuville, 2017), they strongly affect properties such as $S^{conf}(T_g)$ that are influenced by cationic / molecular interactions and steric hindrance effects (Richet, 1984; Hummel and Arndt, 1985; Neuville and Richet, 1991; Neuville and Mysen, 1996; Maehara et al., 2005; Goldstein, 2011). This agrees with predictions for $S^{conf}(T_g)$. The results in Fig. 10c show a clear effect of melt composition on the $S^{conf}(T_g)$ *versus* R_{Raman} relationship. Such chemical effects also affect C_{FV} (Eq. (2), Fig. 8d). This latter term encompasses local cationic influences on melt free volumes in the Free Volume theory (Cohen and Grest, 1979). As a result, it can be expected that mixing different cations will affect this term, explaining the observation made in Fig. 10d. Results actually suggest a link between C_{FV} and $S^{conf}(T_g)$, as corroborated by a Spearman correlation coefficient, r_s, of 0.86 between the two variables.

Other properties show interesting correlations. Fig. 11 shows the Spearman correlation coefficients between the different variables/properties predicted by i-Melt. We observe high correlations between the parameters of the Free Volume and the VFT equations. For example, B_{FV} and B_{VFT} are highly correlated (r_s = 0.997). While B_e is not strongly correlated with the latter variables, the ratio $B_e/S^{conf}(T_g)$ is (r_s = 0.989 and 0.996 with B_{FV} and B_{VFT}, respectively). B_{FV} and B_{VFT} play the role of some kind of activation energies in Eqs. (2) and (3). They thus are related to the energy barriers opposed to the atomic movements at the root of viscous flow. The ratio $B_e/S^{conf}(T_g)$ also is related to those energy barriers (see below, Eqs. (9), (10)). The strong correlations between R_{Raman} and $B_e/S^{conf}(T_g)$, B_{FV} *and* B_{VFT} (Fig. 11) thus indicates that the SiO_2-Al_2O_3 aluminosilicate network connectivity and topology mostly controls those energy barriers. This may explain the broad correlation between the network topology as quantified by R_{Raman} and the glass transition temperature of alkali aluminosilicate melts, discussed previously (Figs. 10, 11).

Properties in the denominator in Eqs. (1) to (5) show more complex correlations among themselves, and with other variables (Fig. 11). A generally strong correlation is observed between variables in the denominator of Eqs. (1) to (5) and the pre-exponential terms reflecting high temperature viscosity limits, namely A_{VFT}, A_{AM}, A_{FV} and A_e (Fig. 11). For example, r_s = -0.87 for the correlation between $S^{conf}(T_g)$ and A_e, r_s = -0.972 for the correlation between C_{VFT} and A_{VFT}, and r_s = 0.80 for that between A_{AM} and the fragility, m. This reflects a numerical correlation between the pre-exponential terms and the denominators of viscosity Eqs. (1)–(5). A way to avoid such correlations, which can bias calculations, is to set the A_{VFT}, A_{AM}, A_{FV} and A_e pre-exponential terms to composition-independent values. Such practice agrees with the general idea that there is a common high temperature viscosity limit (Shaw, 1972; Persikov, 1991; Russell et al., 2003; Giordano et al., 2008; Russell and Giordano, 2017). However, this can be questioned for alkali aluminosilicate melts. Indeed, the study of Robert et al. (2019) suggests that, for alkali tectosilicate melts, A_e could vary as a function of the melt Al/Si ratio. This agrees with earlier findings of Toplis (1998), who showed that A_e actually varies as a function of the ratio B_e/(Al + Si) for various alkali and alkaline earth melt compositions. In the present model, A_{VFT}, A_e, A_{FV} or A_{AM} are allowed to vary with melt composition, such that we can check if the model corroborates the findings of Robert et al. (2019) and Toplis (1998). In Fig. 12a, we observe that, for compositions covering a wide compositional field of the glass forming domain (see inset in Fig. 12b), values of A_e range between ~−1.0 and ~−2.5 $\log_{10}$ Pa·s, those of A_{FV} between ~−2.0 and ~−3.5 $\log_{10}$

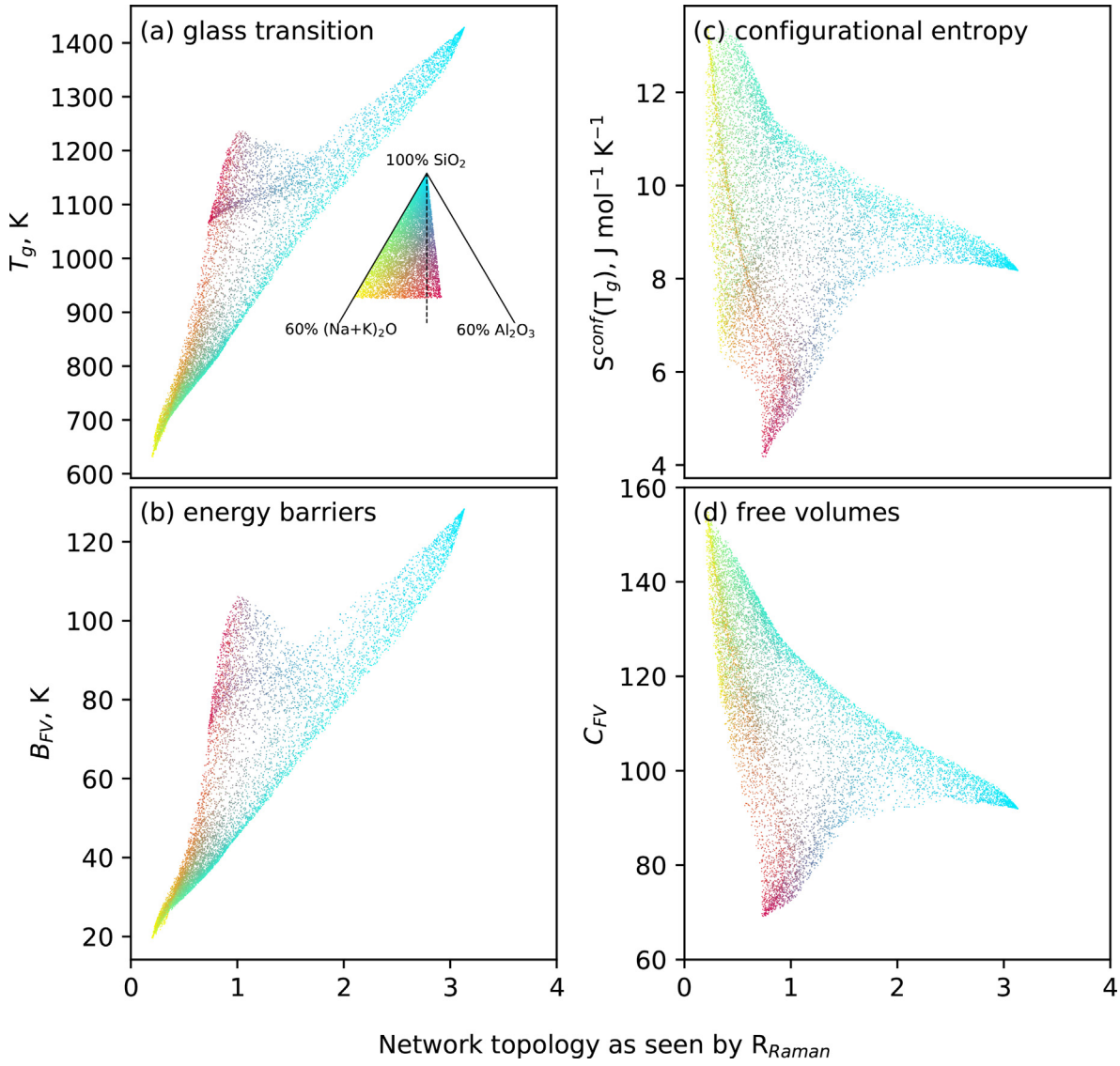

Fig. 10. Melt and glass properties vary in a complex way with glass network topology. i-Melt reveals that parameters such as (a) the viscous glass transition temperature T_g and (b) B_{FV}, an activation energy term in the Free Volume theory (Eq. (2)), correlate broadly with R_{Raman}. Other terms also show more complex variations, influenced by cationic mixing interactions and steric hindrance effects, such as the glass configurational entropy $S^{conf}(T_g)$ (c) or the free volume parameter C_{FV} (d). Each symbol represents the calculation for a randomly generated composition (n = 10,000) in the glass-forming domain of the Na_2O-K_2O-Al_2O_3-SiO_2 system (Fig. 1).

Pa·s, those of A_{AM} between ~−0.2 and ~−1.0 $\log_{10}$ Pa·s, and those of A_{VFT} between ~−6.0 and −3.7 $\log_{10}$ Pa·s. The distributions of those parameters are asymmetric and complex. A_e and A_{VFT} clearly are trimodal, while A_{FV} and A_{AM} distributions are asymmetric and present sharp terminations on one of their side. This suggests the existence of complex compositional effects. Fig. 12b corroborates this idea, and actually the findings of Robert et al. (2019). There is a general effect of the melt Al/Si ratio on the value of A_e. A_{FV} also shows variations that correlate, albeit in a complex manner, with Al/Si, while A_{AM} does not show systematic variations with Al/Si (not shown). Those results thus corroborate the suggestion that for melts in ternary and quaternary systems, the pre-exponential terms in Eqs. (1) and (2) may slightly depend on compositions, and particularly on the Al and Si concentrations and ratios.

4.2. Links between the Adam-Gibbs and the Free Volume theories

The above analysis highlighted important correlations between variables from different theories (Fig. 11). The trans-theoretical character of i-Melt allows us to go further: it allows systematic inference for a given property using different theories, and observation of the relationship between the latent variables of these theories. Here, we are interested in exploring the links between the Adam-Gibbs and Free

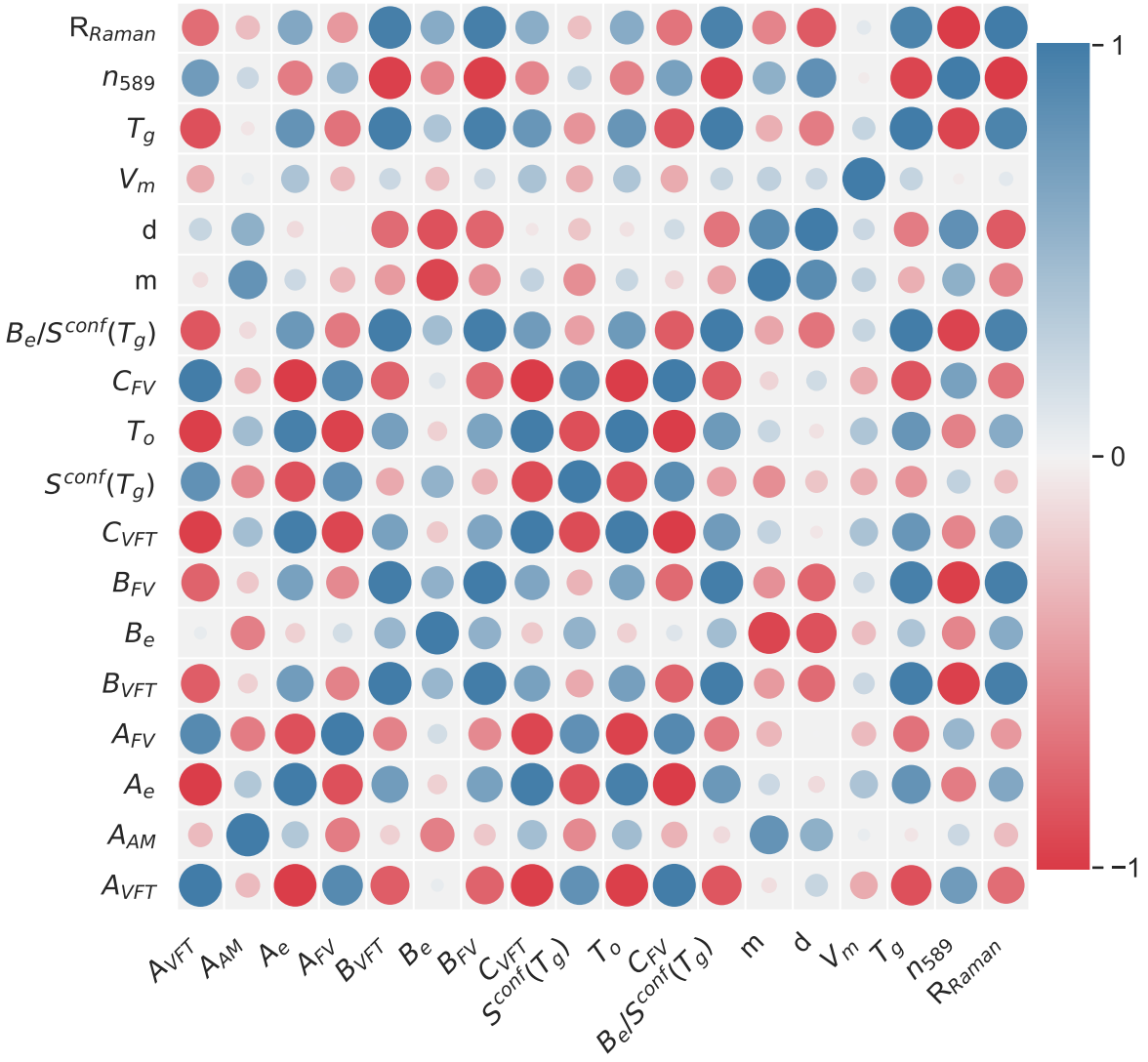

Fig. 11. Spearman correlation matrix between the different variables predicted by i-Melt or calculated from those predictions. The large the circles, the larger the correlation. A correlation of 1 or −1 means a perfect monotonic (possibly non linear) correlation. Spearman correlation coefficients were calculated from the predictions for the 10,000 randomly generated composition in the glass-forming domain of the Na_2O-K_2O-Al_2O_3-SiO_2 system (inset in Fig. 10).

Volume theories to test the proposition of Hodge (1994): it should be possible to build a Free Volume version of the Adam-Gibbs theory.

In the Free Volume theory, solid-like and liquid-like molecular cells are distinguished and separated by a critical volume, v^*. Viscous flow occurs via cooperative molecular movements between liquid-like cells. In the Adam-Gibbs theory, viscous flow occurs via cooperative motions of molecular segments of a size $z^*(T)$, characterized by an intrinsic entropy S_c^*. The two theories thus share common philosophical underpinnings, including the important assumption that viscous flow occurs via cooperative movements of molecular entities in the melt. This relationship can be recognized upon consideration of the parameters of Eqs. (1) and (2). Indeed, B_{FV} embeds some structural information because it depends on v^*:

$$\mathrm{B_{FV}} = \mathrm{v^* z_o}, \tag{9}$$

where z_o is an adjustable parameter. Similarly, the ratio $B_e/S^{conf}(T_g)$ embeds molecular subunit length-scale information as (Toplis, 1998)

$$\mathrm{B_e/S^{conf}(T_g)} = \left[\Delta\mu\ \mathrm{z^*(T_g)}\right]/\mathrm{R}, \tag{10}$$

with $\Delta\mu$ the energy barriers opposed to the rearrangement of molecular subunits of size $z^*(T_g)$, and R the perfect gas constant. We can consider v^* and z^* as structural parameters embedding information about the volume or length-scale of the cooperative molecular regions. Therefore, these parameters should both depend on melt or glass structure. This is confirmed by the fact that both B_{FV} and $B_e/S^{conf}(T_g)$ correlate well with R_{Raman} (Fig. 11). This finding supports the idea that it should be possible to develop a

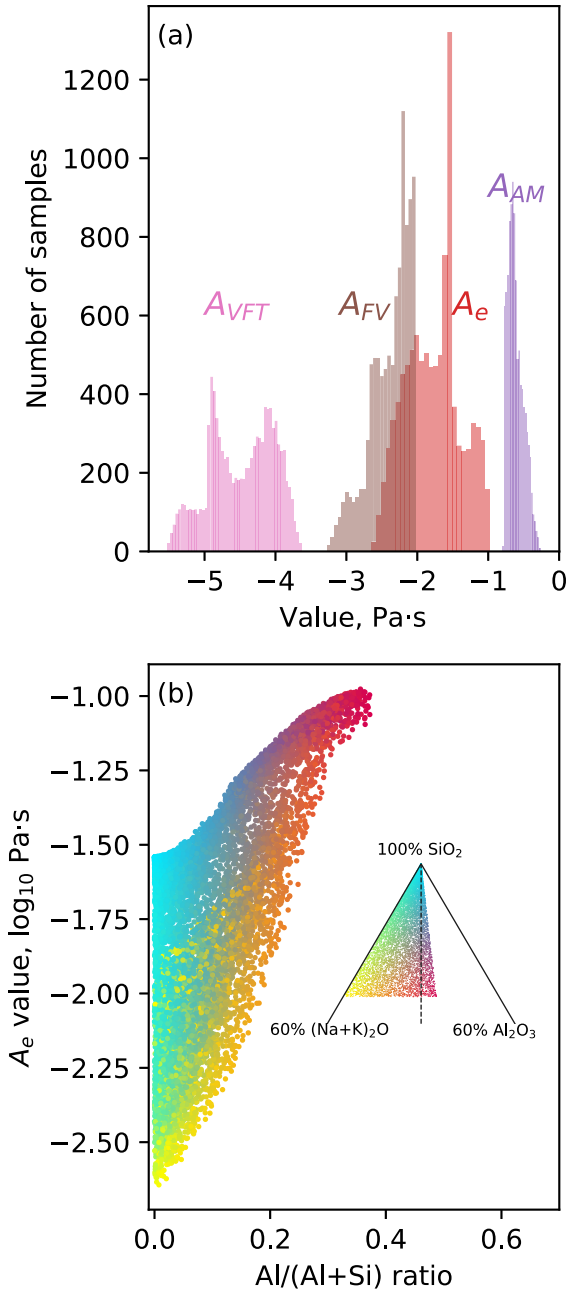

Fig. 12. High temperature viscosity limit. (a) histograms of the high temperature viscosity limits A_{VFT}, A_e, A_{FV} and A_{AM} predicted for 10,000 melt composition randomly selected from the glass-forming domain of the Na_2O-K_2O-Al_2O_3-SiO_2 system. (b) A_e *versus* Al/(Al + Si) diagram highlighting a possible compositional dependence of A_e. The ternary diagram shows again the randomly selected compositions.

Free Volume version of the Adam-Gibbs theory (Hodge, 1994; Liu et al., 2015). More generally, the links between B_{FV}, $B_e/S^{conf}(T_g)$ and R_{Raman} support the general hypothesis that melt viscous flow occurs when a critical molecular length-scale is reached. This length-scale can be indirectly observed through Raman signals (Fig. 10b) and strongly influences the glass transition temperature T_g (Fig. 10a).

4.3. Structure and properties of alkali-rich molten lavas

4.3.1. Influence on the eruptive dynamics of silicic volcanoes

One question that motivated the implementation of i-Melt is: why, in terms of melt structure and properties, are eruptions of silicic volcanoes found to be more explosive when the rhyolite melt is rich in K and Al (Di Genova et al., 2017). Indeed, the compositions of silicic lavas compiled by Di Genova et al. (2017), form two clusters when viewed in terms of the rheological agpaitic index ($[Na^+ + K^+ + Ca^{2+} + Mg^{2+} + Fe^{2+}] / [Fe^{3+} + Al^{3+}]$) and K/(K + Na) ratios, associated with effusive and explosive eruptions (Fig. 13a). According to Di Genova et al. (2017), this correlation seems to stand regardless of the many other critical parameters driving the dynamics of volcanic eruptions, such as pre-eruptive volatile content, degassing path or nanolite content (e.g., Villemant and Boudon, 1998; Andújar and Scaillet, 2012; Di Genova et al., 2017, 2020; Moitra et al., 2018; Cáceres et al., 2020). The eruptive style of rhyolite eruptions thus seems influenced by small variations in magma composition, linked to the influence of potassium and trivalent cations (Al^{3+} mainly, but also Fe^{3+}) on the silicate melt rheology.

Most of the lavas emitted at silicic volcanic systems, such as Yellowstone or Long Valley (U.S.A.), contain more than 95% of Na_2O, K_2O, Al_2O_3 and SiO_2. Therefore, melts in the Na_2O-K_2O-Al_2O_3-SiO_2 system may be considered as simplified analogues of the lavas involved in silicic volcanic eruptions, and i-Melt can be used to glimpse the links between eruptive dynamics and the composition, structure, and properties of magmas. Of course, this will not take the effect of volatile elements into account, but, as highlighted previously, the correlation reported by Di Genova et al. (2017) is actually apparently independent of melt water content. In any case, the following should be considered with care as i-Melt remains limited to a simple quaternary system. In the future, more complete versions of models such as i-Melt will allow more robust exploration of the links between eruptive dynamics and the composition, structure, and properties of magmas.

i-Melt reveals that the two data point clusters observed in Fig. 13a are associated with different $S^{conf}(T_g)$ values. One data point cluster, associated with explosive eruptions, contains $S^{conf}(T_g)$ values typically below ~9 J mol^{-1} K^{-1}, while the other cluster, associated with effusive eruptions, incorporates values above this threshold. Those $S^{conf}(T_g)$ variations indicate that decreasing the rheological agpaitic index and increasing K/(K + Na) leads to fewer available configurations available for viscous flow molecular movements. This results in increasing the melt viscosity, explaining potentially the volcanic eruptive style chemical clustering observed in Fig. 13a.

To go further, we can look at what happens when the composition of a rhyolite shifts from a sodic peralkaline one to a potassic peraluminous one (pink-cyan line in Fig. 13a). Such a shift is accompanied by important changes in melt structure. In particular, predicted Raman spectra show the apparition of a depolymerized Q^3 unit signal in peralkaline melts, while this signal is barely present in peraluminous melts (Fig. 13b). Following the methodology

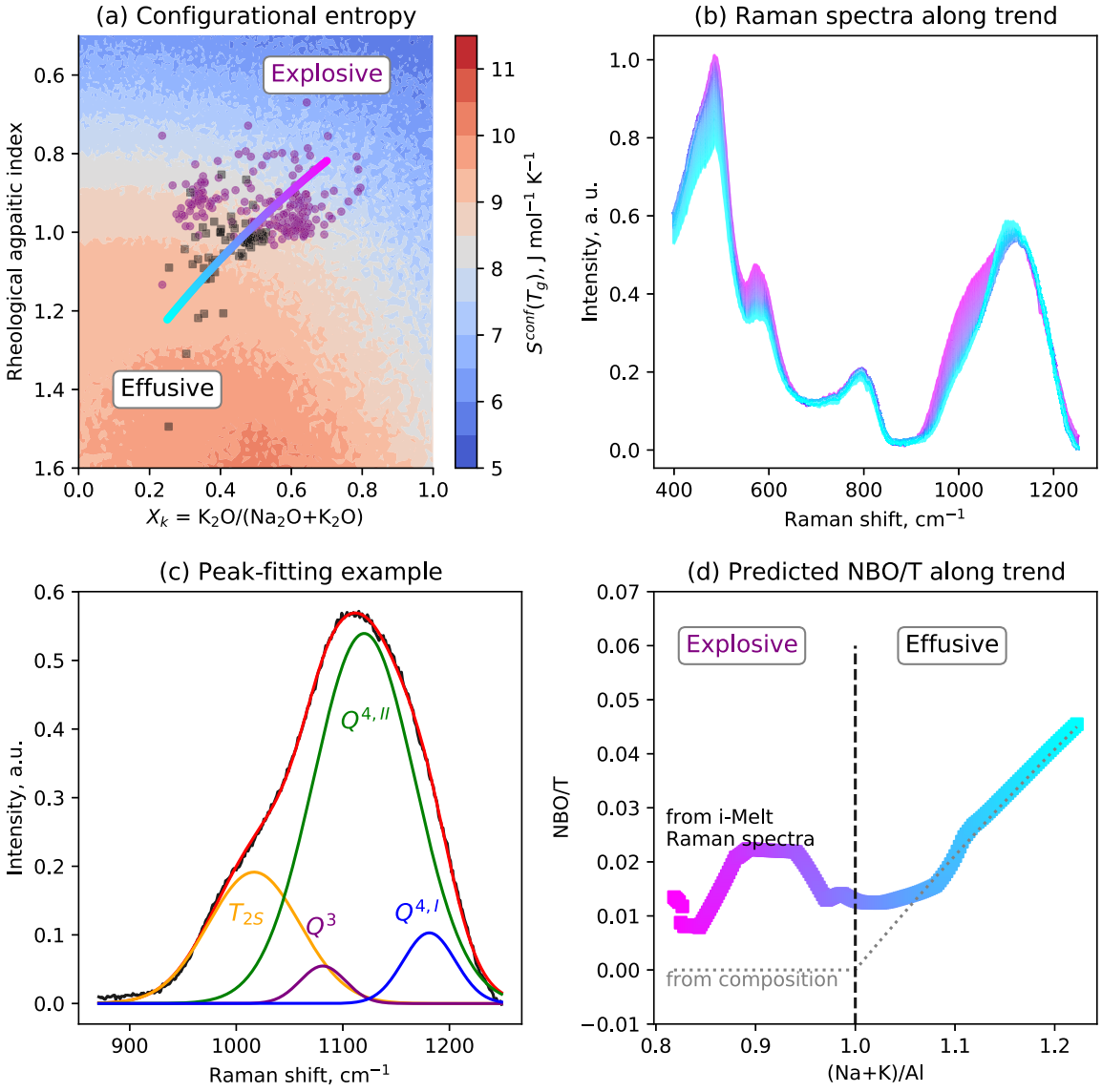

Fig. 13. Influence of Al and K/(K + Na) ratios on rhyolite structure and properties. (a) configurational entropy maps as a function of the ratio K/(K + Na) and the rheological agpaitic index, calculated as ($Na_2O + K_2O + CaO + MgO + FeO$)/($Al_2O_3 + Fe_2O_3$). On top of the maps, symbols of rhyolite effusive (purple circles) and explosive (black squares) eruptions from Di Genova et al. (2017) are represented. Some scatter in the $S^{conf}(T_g)$ contour map is visible and results from model noise. The cyan to pink line is a compositional transect used in (b) to (d). (b) Raman spectra predicted for melts along the cyan-pink transect shown in (a). (c) Example of peak-fitting of the Raman spectra with four gaussian peaks (see text). (d) Evolution of the NBO/T calculated from melt composition (dashed grey line) and from Q^3 peak areas, converted using the Q^3 Raman cross-section from Mysen (2007).

developed in previous studies (Seifert et al., 1982; Neuville and Mysen, 1996; Le Losq and Neuville, 2013; Le Losq et al., 2014), the spectra can be modeled with four bands, assigned to Si—O asymmetric vibrations (T_{2S}), Si—O stretching in Q^3 units and Si-O stretching in two types of Q^4 units (Fig. 13c). While the structure of peraluminous melts is dominated by tightly bonded Q^4 units, as shown by strong intensity near 500 cm^{-1} (Fig. 13b), that of peralkaline melts sees the apparition of Q^3 units (Fig. 13c) that testify for the depolymerization of the melt as the ratio (Na + K)/Al becomes higher than 1 and as alkali elements start to play a network modifier role. As a consequence, the calculated NBO/T increases significantly in peralkaline melts as the (Na + K)/Al ratio increases above 1 (Fig. 13d). The transition observed in Fig. 13a thus seems mostly related to the importance of the absence/presence of non-bridging oxygens in the melt structure, and to their influence on melt properties.

Observations made with i-Melt thus bring important pieces of information: (i) while the configurational entropy varies rather smoothly when going from peralkaline to peraluminous melts (Fig. 13a), the structure changes substantially with the onset of Q^3 units (Fig. 13b–d), and (ii) as already identified by Di Genova et al. (2017), the role of aluminum is more important than that of potassium: most of the variance in Fig. 13a is actually associated with variations in the rheological agpaitic index. The structural and thermodynamic variations, observed in Fig. 13, are associated with very important changes in term of melt viscosity. Indeed, the compositional change forming the trend shown in Fig. 13a (pink-cyan line) is accompanied by a change of the viscosity of more than three orders of magnitudes at 1000 °C (Supplementary Fig. 4).

The above discussion allows understanding structural, thermodynamic and rheological changes possibly at the source of the effusive/explosive clustering observed in Fig. 13a. However, one should remember that, here, only a simplified system is considered. Other variables, such as melt water and iron contents, may have important, and possibly indirect, roles too in the correlation observed in Fig. 13a. For instance, an increase in the Al/(Na + K) ratio of aluminosilicate melts, in addition to strongly affecting melt polymerization and properties, promotes iron reduction (Dickenson and Hess, 1982). Such a phenomenon could promote the rapid appearance of iron-bearing nanolites, and hence act as an accelerator in the increase of magma viscosity to promote the explosivity of the eruption (Di Genova et al., 2017, 2020; Cáceres et al., 2020).

4.3.2. K/Na ratio and the properties of magmas along alkaline magmatic series

In addition to rhyolites, melts along a basanite-phonolite differentiation trend typically show high concentrations of sodium and potassium. The properties of such melts could, therefore, be affected by the different impact of Na and K on the melt structure and properties. To test this idea, it is possible to use i-Melt to study the influence of the K/(K + Na) ratio on the properties and structure of basanite-like to phonolite-like simplified melt compositions. Here, we simulate how the properties of a melt change when it evolves from an initial composition with 55 mol% SiO_2 and $Al_2O_3/SiO_2 = 0.18$ to a final composition with 67 mol% SiO_2 and $Al_2O_3/SiO_2 = 0.20$. The K/(K + Na) of the sodic trend is fixed at 0.33, and that of the potassic trend at 0.66. NBO/T of the melts will evolve from 0.63 down to 0.13, such values being reflective of those typical of a basanite-phonolite trend.

Simulating the properties of the melts along such a basanite-like to phonolite-like evolution trend, we observe a systematically higher viscosity of the potassic melts (Fig. 14a); the most mafic melts show a difference of ~0.5 $\log_{10}$ unit, while the most evolved melts display a viscosity difference of more than an order of magnitude. The prediction of the Raman spectra of the quenched melts along the two differentiation trends also show systematic differences. We observe that the decrease in NBO/T upon melt differentiation is accompanied by decreasing Q^3 and Q^2 Raman signals for both series (Fig. 14b, c). However, K-rich melts

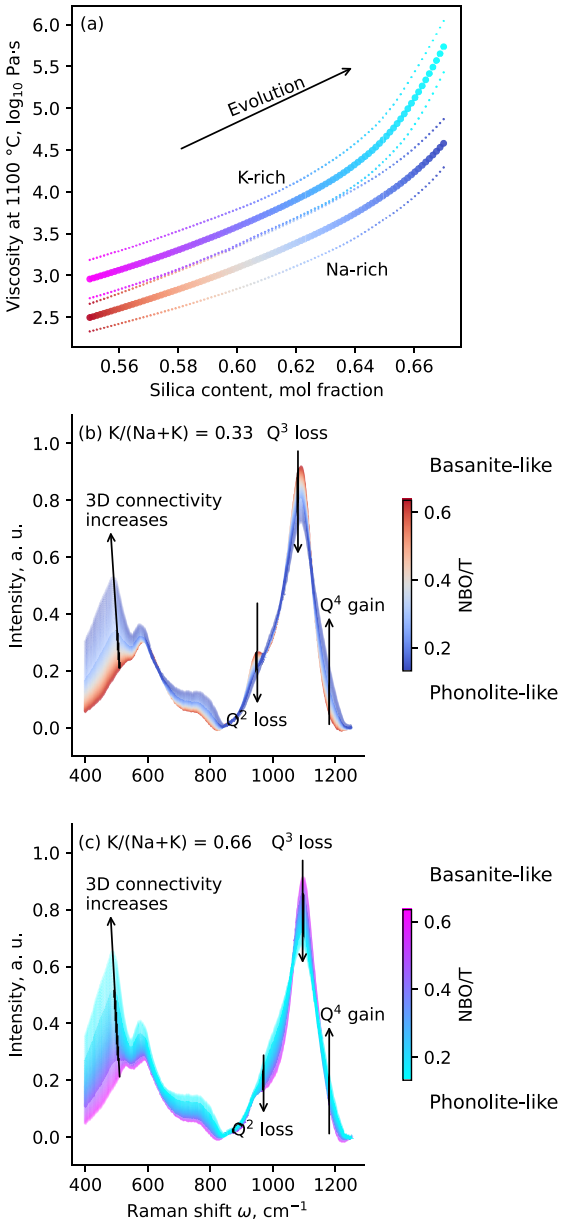

Fig. 14. Influence of the K/(K + Na) ratio on the viscosity and atomic structure of alkali aluminosilicate melts, mimicking the evolution from a basanite-like mafic pole to a phonolite-like pole. (a) Viscosity ($\log_{10}$ Pa·s) at 1100 °C of the melts as a function of their silica mol fraction. Two trends are visible for Na-rich melts with K/(K + Na) = 0.33, and K-rich melts with K/(K + Na) = 0.66. (b) and (c) Predicted evolution of the Raman spectra of Na-rich and K-rich melt compositions, respectively. Mean predictions are generated feeding the 10 models with 100 melt compositions generated linearly between the end-member poles (see text for details).

appear systematically richer in Q^3 units, and depleted in Q^2 units compared to Na-rich melts. This is expected because the equilibrium constant of the reaction $2Q^3 = Q^2 + Q^4$ is higher in K-rich silicate melts than in Na-rich silicate melts (Maekawa et al., 1991). We further observe stronger signals in the 400–600 cm^{-1} region in

K-rich phonolite-like melts, providing evidence for a higher Q^n-Q^n interconnection, in agreement with their higher viscosity.

From those results, the K/(Na + K) ratio along a basanite-phonolite differentiation trend may play a role on the properties of the magmas, and, ultimately on the eruptive dynamics at surface. However, it should be reminded that water content is the primary factor linked to the effusive/explosive dynamics of eruptions involving phonolite melts (Andújar and Scaillet, 2012). Therefore, we expect the K/(Na + K) ratio to play a secondary role compared to water content. However, this role is not insignificant, particular given the strong influence of melt K/(Na + K) on various parameters such as the iron redox state (Cicconi et al., 2015), the diffusion and solubility of volatile elements like F and Cl (Balcone-Boissard et al., 2009; Dalou et al., 2015) or the speciation and solubility of dissolved water (e.g., Behrens et al., 2001; Le Losq et al., 2015). In conjunction with the potential influence of K/(Na + K) on Fe-free and volatile-free melt structure and properties (Fig. 14), this invites further studies of the differences in terms of eruptive mechanisms and dynamics between Na-rich and K-rich alkaline magma series. In particular, the hypothesis that K-rich alkaline magma series may be linked more frequently to explosive dynamics can be proposed and should be tested.

5. CONCLUSION

i-Melt, a model integrating a feed-forward neural network and physical equations, was developed to predict alkali aluminosilicate melt and glass properties, including configurational entropy, glass transition temperature, fragility, viscosity, density, optical refractive index and Raman spectra. The model allows making predictions with a good precision in the glass forming domain. Extrapolations are possible but should be done with care. We see models like i-Melt, therefore, as a pragmatic compromise between informative, accurate but limited theoretical models and mono-task empirical models. i-Melt can readily be extended to include quantities of interest across a range of domains and applications, including glass toughness and hardness. In general, the present results show that the possibility of combining machine learning with physical and thermodynamic models offers exciting new perspectives.

Applied to rhyolite compositions, i-Melt reveals that the reported chemical tipping point between effusive and explosive eruptions is largely linked to the disappearance of non-bridging oxygens in Al-rich compositions, which lowers melt configurational entropy and triggers a strong increase in melt viscosity. Results on simplified alkaline magmatic series further indicate that K-rich melts present systematically higher viscosities, being linked to slight differences in the atomic structure as suggested by the predicted Raman spectra of the glasses. When considering this result together with the other reported effects of the K/(K + Na) ratio on iron redox state, volatile solubility, speciation and diffusivity in phonolitic melts, it can be expected that Na-rich or K-rich alkaline magmatic series may be associated with slightly different eruptive dynamics.

Declaration of Competing Interest

The authors declare that they have no known competing financial interests or personal relationships that could have appeared to influence the work reported in this paper.

ACKNOWLEDGMENTS

CLL thanks Malcolm Sambridge (Seismology & Mathematical Geophysics, RSES, Australian National University), Lexing Xie and Cheng Soon Ong (CECS, Australian National University), for various discussions and their advice regarding optimization and machine learning. Constructive comments and criticisms from three anonymous reviewers, Associate Editor Sung Keun Lee and Executive Editor Jeffrey G. Catano were highly appreciated and clearly helped improving the quality of the manuscript and computer code. CLL also thanks G. Dreyfus (ESPCI-ParisTech) for helpful comments on the pre-proofs. Numerical computations were partly performed on the S-CAPAD plateforme, IPGP, France.

FUNDING

CLL acknowledges funding from a Chaire d'Excellence IDEX19C627X/FD070/D110 from the ANR IdEX Université de Paris 18-IDEX-0001, from the Australian Research Council Laureate Fellowship FL130100066 to Prof. Hugh O'Neill (ANU-RSES) as well as from the Postdoctoral Fellowship of the Carnegie Institution for Science during the realization of this project. APV acknowledges support from the ARC via grants DE180100040 and DP200100053.

AUTHOR CONTRIBUTIONS

CLL designed the study, collected the data, performed Raman and viscosity experiments, and developed the deep learning framework and the associated computer code. AV and BOM helped in the design of the neural network. CLL and AV worked on improving and testing of the computer code. CLL, BOM and DN performed Raman measurements. CLL and AV drafted the manuscript. All authors contributed to the final version of the manuscript.

Materials & Correspondence: All the data are available in the main text or the supplementary materials. The computer code to reproduce the results of this study is available as a Python library at the web address https://github.com/charlesll/i-melt. Correspondence can be addressed to the corresponding author.

APPENDIX A. SUPPLEMENTARY MATERIAL

Supplementary data to this article can be found online at https://doi.org/10.1016/j.gca.2021.08.023.

REFERENCES

Adam G. and Gibbs J. H. (1965) On the temperature dependence of cooperative relaxation properties in glass-forming liquids. *J. Chem. Phys.* **43**, 139–146.

Allu A. R., Gaddam A., Ganisetti S., Balaji S., Siegel R., Mather G. C., Fabian M., Pascual M. J., Ditaranto N., Milius W., Senker J., Agarkov D. A., Kharton Vladislav V. and Ferreira J. M. F. (2018) Structure and crystallization of alkaline-earth aluminosilicate glasses: prevention of the alumina-avoidance principle. *J. Phys. Chem. B* **122**, 4737–4747.

Allwardt J. R., Poe B. T. and Stebbins J. F. (2005a) The effect of fictive temperature on Al coordination in high-pressure (10 GPa) sodium aluminosilicate glasses. *Am. Mineral.* **90**, 1453–1457.

Allwardt J. R., Stebbins J. F., Schmidt B. C., Frost D. J., Withers A. C. and Hirschmann M. M. (2005b) Aluminum coordination and the densification of high-pressure aluminosilicate glasses. *Am. Mineral.* **90**, 1218–1222.

Ando M. F., Benzine O., Pan Z., Garden J.-L., Wondraczek K., Grimm S., Schuster K. and Wondraczek L. (2018) Boson peak, heterogeneity and intermediate-range order in binary SiO_2-Al_2O_3 glasses. *Sci. Rep.*, 8.

Andújar J. and Scaillet B. (2012) Relationships between pre-eruptive conditions and eruptive styles of phonolite–trachyte magmas. *Lithos* **152**, 122–131.

Avramov I. (2011) Dependence of the parameters of equations of viscous flow on chemical composition of silicate melts. *J. Non-Cryst. Solids* **357**, 3841–3846.

Avramov I. and Milchev A. (1988) Effect of disorder on diffusion and viscosity in condensed systems. *J. Non-Cryst. Solids* **104**, 253–260.

Balcone-Boissard H., Baker D. R., Villemant B. and Boudon G. (2009) F and Cl diffusion in phonolitic melts: influence of the Na/K ratio. *Chem. Geol.* **263**, 89–98.

Bancroft G. M., Nesbitt H. W., Henderson G. S., O'Shaughnessy C., Withers A. C. and Neuville D. R. (2018) Lorentzian dominated lineshapes and linewidths for Raman symmetric stretch peaks (800–1200 cm^{-1}) in Q^n (n = 1–3) species of alkali silicate glasses/melts. *J. Non-Cryst. Solids* **484**, 72–83.

Bauchy M., Guillot B., Micoulaut M. and Sator N. (2013) Viscosity and viscosity anomalies of model silicates and magmas: a numerical investigation. *Chem. Geol.* **346**, 47–56.

Bechgaard T. K., Mauro J. C., Bauchy M., Yue Y., Lamberson L. A., Jensen L. R. and Smedskjaer M. M. (2017) Fragility and configurational heat capacity of calcium aluminosilicate glass-forming liquids. *J. Non-Cryst. Solids* **461**, 24–34.

Beckner W., Mao M. C. and Pfaendtner J. (2018) Statistical models are able to predict ionic liquid viscosity across a wide range of chemical functionalities and experimental conditions. *Mol. Syst. Des. Eng.* **3**, 253–263.

Behrens H., Meyer M., Holtz F., Benne D. and Nowak M. (2001) The effect of alkali ionic radius, temperature and pressure on the solubility of water in $MAlSi_3O_8$ melts (M=Li, Na, K, Rb). *Chem. Geol.* **174**, 275–289.

Bell R. J., Bird N. F. and Dean P. (1968) The vibrational spectra of vitreous silica, germania and beryllium fluoride. *J. Phys. C Proc Phys Soc* **1**, 299–303.

Bergstra J. and Bengio Y. (2012) Random search for hyper-parameter optimization. *J. Mach. Learn. Res.* **13**, 281–305.

Bishop C. M. (2006) Pattern Recognition and Machine Learning. Springer, New York.

Bockris J. O., MacKenzie J. D. and Kitchener J. A. (1955) Viscous flow in silica and binary liquid silicates. *Trans. Faraday Soc.* **51**, 1734–1748.

Bottinga Y. and Richet P. (1996) Silicate melt structural relaxation: rheology, kinetics, and Adam-Gibbs theory. *Chem. Geol.* **128**, 129–141.

Bottinga Y., Richet P. and Sipp A. (1995) Viscosity regimes of homogeneous silicate melts. *Am. Mineral.* **80**, 305–318.

Bottinga Y. and Weill D. F. (1972) The viscosity of magmatic silicate liquids: a model for calculation. *Am. J. Sci.* **272**, 438–475.

Bowen N. L. (1928) The Evolution of Igneous Rocks. Oxford University Press.

Brawer S. A. and White W. B. (1975) Raman spectroscopic investigation of the structure of silicate glasses. I. The binary alkali silicates. *J. Chem. Phys.* **63**, 2421–2432.

Brawer S. A. and White W. B. (1977) Raman spectroscopic investigation of the structure of silicate glasses (II). Soda-alkaline earth-alumina ternary and quaternary glasses. *J. Non-Cryst. Solids* **23**, 261–278.

Breiman L. (1996) Bagging predictors. *Mach. Learn.* **24**, 123–140.

Cáceres F., Wadsworth F. B., Scheu B., Colombier M., Madonna C., Cimarelli C., Hess K.-U., Kaliwoda M., Ruthensteiner B. and Dingwell D. B. (2020) Can nanolites enhance eruption explosivity?. *Geology* **48** 997–1001.

Caruana R. (1997) Multitask Learning. *Mach. Learn.* **28**, 41–75.

Cassar D. R. (2021) ViscNet: neural network for predicting the fragility index and the temperature-dependency of viscosity. *Acta Mater.* **206**, 116602.

Cassidy M., Manga M., Cashman K. and Bachmann O. (2018) Controls on explosive-effusive volcanic eruption styles. *Nat. Commun.* **9**, 2839.

Cicconi M. R., Giuli G., Ertel-Ingrisch W., Paris E. and Dingwell D. B. (2015) The effect of the [Na/(Na+K)] ratio on Fe speciation in phonolitic glasses. *Am. Mineral.* **100**, 1610–1619.

Cohen M. H. and Grest G. S. (1979) Liquid-glass transition, a free-volume approach. *Phys. Rev. B* **20**, 1077.

Cohen M. H. and Grest G. S. (1984) The nature of the glass transition. *J. Non-Cryst. Solids* **61–62**, 749–759.

Dalou C., Le Losq C., Mysen B. O. and Cody G. D. (2015) Solubility and solution mechanisms of chlorine and fluorine in aluminosilicate melts at high pressure and high temperature. *Am. Mineral.* **100**, 2272–2283.

Day D. E. (1976) Mixed alkali glasses - Their properties and uses. *J. Non-Cryst. Solids* **21**, 343–372.

Di Genova D., Brooker R. A., Mader H. M., Drewitt J. W. E., Longo A., Deubener J., Neuville D. R., Fanara S., Shebanova O., Anzellini S., Arzilli F., Bamber E. C., Hennet L., La Spina G. and Miyajima N. (2020) In situ observation of nanolite growth in volcanic melt: a driving force for explosive eruptions. *Sci. Adv.* **6**, eabb0413.

Di Genova D., Kolzenburg S., Wiesmaier S., Dallanave E., Neuville D. R., Hess K. U. and Dingwell D. B. (2017) A compositional tipping point governing the mobilization and eruption style of rhyolitic magma. *Nature* **552**, 235.

Diallo B., Allix M., Véron E., Sarou-Kanian V., Bardez-Giboire I., Montouillout V. and Pellerin N. (2019) Deconvolution method of ^{29}Si MAS NMR spectra applied to homogeneous and phase separated lanthanum aluminosilicate glasses. *J. Non-Cryst. Solids* **503–504**, 352–365.

Dickenson M. P. and Hess P. C. (1982) Redox equilibria and the structural role of iron in alumino-silicate melts. *Contrib. Miner. Petrol.* **78**, 352–357.

Dingwell D. B. (1996) Volcanic dilemma – flow or blow? *Science* **273**, 1054–1055.

Drewitt J. W. E., Jahn S., Sanloup C., de Grouchy C., Garbarino G. and Hennet L. (2015) Development of chemical and topological structure in aluminosilicate liquids and glasses at high pressure. *J. Phys.: Condens. Matter* **105103**.

Dreyfus C. and Dreyfus G. (2003) A machine learning approach to the estimation of the liquidus temperature of glass-forming oxide blends. *J. Non-Cryst. Solids* **318**, 63–78.

Duan X. (2014) A model for calculating the viscosity of natural iron-bearing silicate melts over a wide range of temperatures, pressures, oxygen fugacites, and compositions. *Am. Mineral.* **99**, 2378–2388.

Dufils T., Folliet N., Mantisi B., Sator N. and Guillot B. (2017) Properties of magmatic liquids by molecular dynamics simulation: the example of a MORB melt. *Chem. Geol.* **461**, 34–46.

Dufils T., Sator N. and Guillot B. (2020) A comprehensive molecular dynamics simulation study of hydrous magmatic liquids. *Chem. Geol.* **533**, 119300.

Furukawa T., Fox K. E. and White W. B. (1981) Raman spectroscopic investigation of the structure of silicate glasses. III. Raman intensities and structural units in sodium silicate glasses. *J. Chem. Phys.* **75**, 3226–3237.

Giordano D. and Russell J. K. (2017) The heat capacity of hydrous multicomponent natural melts and glasses. *Chem. Geol.* **461**, 96–103.

Giordano D. and Russell J. K. (2018) Towards a structural model for the viscosity of geological melts. *Earth Planet. Sci. Lett.* **501**, 202–212.

Giordano D., Russell J. K. and Dingwell D. B. (2008) Viscosity of magmatic liquids: a model. *Earth Planet. Sci. Lett.* **271**, 123–134.

Glorot X., Bordes A. and Bengio Y. (2011) Deep sparse rectifier neural networks. In *International Conference on Artificial Intelligence and Statistics*, pp. 315–323.

Goldstein M. (2011) On the reality of the residual entropy of glasses and disordered crystals: the entropy of mixing. *J. Non-Cryst. Solids* **357**, 463–465.

Gonnermann H. M. (2015) Magma fragmentation. *Annu. Rev. Earth Planet. Sci.* **43**, 431–458.

Gonnermann H. M. and Manga M. (2013) Dynamics of magma ascent in the volcanic conduit. Cambridge University Press, pp. 55–84.

Goodfellow I., Bengio Y. and Courville A. (2016) Deep Learning. MIT Press.

Guillot B. and Sator N. (2007) A computer simulation study of natural silicate melts. Part I: Low pressure properties. *Geochim. Cosmochim. Acta* **71**, 1249–1265.

Herzog F. and Zakaznova-Herzog V. P. (2011) Quantitative Raman spectroscopy: Challenges, shortfalls, and solutions - Application to calcium silicate glasses. *Am. Mineral.* **96**, 914–927.

Hess K. U. and Dingwell D. D. (1996) Viscosities of hydrous leucogranitic melts: A non-Arrhenian model. *Am. Mineral.* **81**, 1297–1300.

Hodge I. M. (1994) Enthalpy relaxation and recovery in amorphous materials. *J. Non-Cryst. Solids* **169**, 211–266.

Hui H. and Zhang Y. (2007) Toward a general viscosity equation for natural anhydrous and hydrous silicate melts. *Geochim. Cosmochim. Acta* **71**, 403–416.

Hummel W. and Arndt J. (1985) Variation of viscosity with temperature and composition in the plagioclase system. *Contrib. Miner. Petrol.* **90**, 83–92.

Hwang J., Tanaka Y., Ishino S. and Watanabe S. (2020) Prediction of viscosity behavior in oxide glass materials using cation fingerprints with artificial neural networks. *Sci. Technol. Adv. Mater.* **21**, 492–504.

Isard J. O. (1969) The mixed alkali effect in glass. *J. Non-Cryst. Solids* **1**, 235–261.

Iuga D., Morais C., Gan Z., Neuville D. R., Cormier L. and Massiot D. (2005) NMR heteronuclear correlation between quadrupolar nuclei in solids. *J. Am. Chem. Soc.* **127**, 11540–11541.

Jackson W. E., Brown G. E. and Ponader C. W. (1987) X-ray absorption study of the potassium coordination environment in glasses from the $NaAlSi_3O_8$-$KAlSi_3O_8$ binary. *J. Non-Cryst. Solids* **93**, 311–322.

Jarry P. and Richet P. (2001) Unmixing in sodium-silicate melts: influence on viscosity and heat capacity. *J. Non-Cryst. Solids* **293–295**, 232–237.

Karpatne A., Watkins W., Read J. and Kumar V. (2018) Physics-guided neural networks (PGNN): an application in lake temperature modeling. *ArXiv171011431 Phys. Stat.*.

Kaufman S., Rosset S., Perlich C. and Stitelman O. (2012) Leakage in data mining: formulation, detection, and avoidance. *ACM Trans. Knowl. Discov. Data* **6**, 1–21.

Kiczenski T. J., Du L.-S. and Stebbins J. (2005) The effect of fictive temperature on the structure of E-glass: a high resolution, multinuclear NMR study. *J. Non-Cryst. Solids* **351**, 3571–3578.

Koroleva O. N., Anfilogov V. N., Shatskiy A. and Litasov K. D. (2013) Structure of Na_2O–SiO_2 melt as a function of composition: In situ Raman spectroscopic study. *J. Non-Cryst. Solids* **375**, 62–68.

Le Losq C. (2018) Rampy: a Python library for processing spectroscopic (IR, Raman, XAS...) data. *Zenodo*. doi.10.5281/zenodo.1168729.

Le Losq C., Berry A. J., Kendrick M. A., Neuville D. R. and O'Neill H. St. C. (2019a) Determination of the oxidation state of iron in Mid-Ocean Ridge basalt glasses by Raman spectroscopy. *Am. Mineral.* **104**, 1032–1042.

Le Losq C., Cicconi M. R., Greaves G. N. and Neuville D. R. (2019b) Silicate Glasses. *Handbook of Glass*. Springer.

Le Losq C., Mysen B. O. and Cody G. D. (2015) Water and magmas: insights about the water solution mechanisms in alkali silicate melts from infrared, Raman, and ^{29}Si solid-state NMR spectroscopies. *Prog. Earth Planet Sci.*, 2.

Le Losq C. and Neuville D. R. (2013) Effect of the Na/K mixing on the structure and the rheology of tectosilicate silica-rich melts. *Chem. Geol.* **346**, 57–71.

Le Losq C. and Neuville D. R. (2017) Molecular structure, configurational entropy and viscosity of silicate melts: link through the Adam and Gibbs theory of viscous flow. *J. Non-Cryst. Solids* **463**, 175–188.

Le Losq C., Neuville D. R., Chen W., Florian P., Massiot D., Zhou Z. and Greaves G. N. (2017) Percolation channels: a universal idea to describe the atomic structure and dynamics of glasses and melts. *Sci. Rep.* **7**, 16490.

Le Losq C., Neuville D. R., Florian P., Henderson G. S. and Massiot D. (2014) The role of Al^{3+} on rheology and structural changes of sodium silicate and aluminosilicate glasses and melts. *Geochim. Cosmochim. Acta* **126**, 495–517.

Lee S. K. (2005) Structure and the extent of disorder in quaternary (Ca-Mg and Ca-Na) aluminosilicate glasses and melts. *Am. Mineral.* **90**, 1393–1401.

Lee S. K., Kim H.-I., Kim E. J., Mun K. Y. and Ryu S. (2016) Extent of Disorder in Magnesium Aluminosilicate Glasses: insights from ^{27}Al and ^{17}O NMR. *J. Phys. Chem. C* **120**, 737–749.

Lee S. K., Mun K. Y., Kim Y.-H., Lhee J., Okuchi T. and Lin J.-F. (2020) Degree of Permanent Densification in Oxide Glasses upon Extreme Compression up to 24 GPa at Room Temperature. *J. Phys. Chem. Lett.* **11**, 2917–2924.

Lee S. K., Mysen B. O. and Cody G. D. (2003) Chemical order in mixed-cation silicate glasses and melts. *Phys. Rev. B* **68**, 214206.

Lee S. K. and Stebbins J. F. (1999) The degree of aluminum avoidance in aluminosilicate glasses. *Am. Mineral.* **84**, 937–945.

Lee S. K., Yi Y. S., Cody G. D., Mibe K., Fei Y. and Mysen B. O. (2012) Effect of network polymerization on the pressure-induced structural changes in sodium aluminosilicate glasses and melts: ^{27}Al and ^{17}O solid-state NMR study. *J. Phys. Chem. C* **116**, 2183–2191.

Lee S. and Stebbins J. (2009) Effects of the degree of polymerization on the structure of sodium silicate and aluminosilicate glasses and melts: an ^{17}O NMR study. *Geochim. Cosmochim. Acta* **73**, 1109–1119.

Liu G., Zhao D. and Zuo Y. (2015) Modified Adam-Gibbs models based on free volume concept and their application in the enthalpy relaxation of glassy polystyrene. *J. Non-Cryst. Solids* **417–418**, 52–59.

Liu H., Fu Z., Yang K., Xu X. and Bauchy M. (2019) Machine learning for glass science and engineering: a review. *J. Non-Cryst. Solids X* **4**, 100036.

Maehara T., Yano T. and Shibata S. (2005) Structural rules of phase separation in alkali silicate melts analyzed by high-temperature Raman spectroscopy. *J. Non-Cryst. Solids* **351**, 3685–3692.

Maekawa H., Maekawa T., Kawamura K. and Yokokawa T. (1991) The structural groups of alkali silicate glasses determined from ^{29}Si MAS-NMR. *J. Non-Cryst. Solids* **127**, 53–64.

Malfait W. J. (2009) Quantitative Raman spectroscopy: speciation of cesium silicate glasses. *J. Raman Spectrosc.* **40**, 1895–1901.

Malfait W. J., Zakaznova-Herzog V. P. and Halter W. E. (2007) Quantitative Raman spectroscopy: high-temperature speciation of potassium silicate melts. *J. Non-Cryst. Solids* **353**, 4029–4042.

Massiot D., Fayon F., Montouillout V., Pellerin N., Hiet J., Roiland C., Florian P., Coutures J., Cormier L. and Neuville D. (2008) Structure and dynamics of oxide melts and glasses: a view from multinuclear and high temperature NMR. *J. Non-Cryst. Solids* **354**, 249–254.

Matson D. W. and Sharma S. K. (1985) Structures of sodium alumino- and gallosilicate glasses and their germanium analogs. *Geochim. Cosmochim. Acta* **49**, 1913–1924.

Mauro J. C., Yue Y., Ellison A. J., Gupta P. K. and Allan D. C. (2009) Viscosity of glass-forming liquids. *Proc. Natl. Acad. Sci.* **106**, 19780–19784.

Mazurin O. V., Streltsina M. V. and Shvaiko-Shvaikovskaya (1987) *Handbook of Glass Data*. Elsevier.

McKeown D. A., Waychunas G. A. and Brown G. E. (1985) EXAFS and XANES study of the local coordination environment of sodium in a series of silica-rich glasses and selected minerals within the Na_2O-Al_2O_3-SiO_2 system. *J. Non-Cryst. Solids* **74**, 325–348.

McMillan P. F. (1984) Structural studies of silicate glasses and melts - Applications and limitations of Raman spectroscopy. *Am. Mineral.* **69**, 622–644.

Merzbacher C. I. and White W. B. (1991) The structure of alkaline earth aluminosilicate glasses as determined by vibrational spectroscopy. *J. Non-Cryst. Solids* **130**, 18–34.

Moitra P., Gonnermann H. M., Houghton B. F. and Tiwary C. S. (2018) Fragmentation and Plinian eruption of crystallizing basaltic magma. *Earth Planet. Sci. Lett.* **500**, 97–104.

Morin E. I., Wu J. and Stebbins J. F. (2014) Modifier cation (Ba, Ca, La, Y) field strength effects on aluminum and boron coordination in aluminoborosilicate glasses: the roles of fictive temperature and boron content. *Appl. Phys. A* **116**, 479–490.

Moseley B., Markham A. and Nissen-Meyer T. (2020) Solving the wave equation with physics-informed deep learning. *ArXiv200611894 Phys.*.

Murphy K. P. (2012) *Machine Learning: A Probabilistic Perspective*. The MIT Press, Cambridge, Massachusetts.

Mysen B. O. (1995) Experimental, in situ, high-temperature studies of properties and structure of silicate melts relevant to magmatic processes. *Eur. J. Mineral.* **7**, 745–766.

Mysen B. O. (1996) Haploandesitic melts at magmatic temperatures: in situ, high-temperature structure and properties of melts along the join $K_2Si_4O_9$-$K_2(KAl)_4O_9$ to 1236°C at atmospheric pressure. *Geochim. Cosmochim. Acta* **60**, 3665–3685.

Mysen B. O. (1991) Relations between structure, redox equilibria of iron, and properties of magmatic liquids. In *Physical Chemistry of Magmas Advances in Physical Geochemistry*. Springer, New York, NY, pp. 41–98.

Mysen B. O. (1990) Role of Al in depolymerized, peralkaline aluminosilicate melts in the systems Li_2O-Al_2O-SiO_2, Na_2O-Al_2O-SiO_2, and K_2O-Al_2O-SiO_2. *Am. Mineral.* **75**, 120–134.

Mysen B. O. (1999) Structure and properties of magmatic liquids: from haplobasalt to haploandesite. *Geochim. Cosmochim. Acta* **63**, 95–112.

Mysen B. O. (1988) *Structure and Properties of Silicate Melts*. W. S. FYFE, Elsevier, Amsterdam-Oxford-New York-Tokyo.

Mysen B. O. (2007) The solution behavior of H_2O in peralkaline aluminosilicate melts at high pressure with implications for properties of hydrous melts. *Geochim. Cosmochim. Acta* **71**, 1820–1834.

Mysen B. O., Finger L. W., Virgo D. and Seifert F. A. (1982a) Curve-fitting of Raman spectra of silicate glasses. *Am. Mineral.* **67**, 686–695.

Mysen B. O. and Frantz J. D. (1992) Raman spectroscopy of silicate melts at magmatic temperatures: Na_2O-SiO_2, K_2O-SiO_2 and Li_2O-SiO_2 binary compositions in the temperature range 25–1475°C. *Chem. Geol.* **96**, 321–332.

Mysen B. O., Lucier A. and Cody G. D. (2003) The structural behavior of Al^{3+} in peralkaline melts and glasses in the system Na_2O-Al_2O_3-SiO_2. *Am. Mineral.* **88**, 1668–1678.

Mysen B. O. and Richet P. (2019) *Silicate Glasses and Melts*, second ed. Elsevier.

Mysen B. O. and Toplis M. J. (2007) Structural behavior of Al^{3+} in peralkaline, metaluminous, and peraluminous silicate melts and glasses at ambient pressure. *Am. Mineral.* **92**, 933–946.

Mysen B. O., Virgo D. and Scarfe C. M. (1980) Relations between the anionic structure and viscosity of silicate melts – a Raman spectroscopic study. *Am. Mineral.* **65**, 690–710.

Mysen B. O., Virgo D. and Seifert F. A. (1982b) The structure of silicate melts: implications for chemical and physical properties of natural magma. *Rev. Geophys.* **20**, 353–383.

Nesbitt H. W., Henderson G. S., Bancroft G. M. and Neuville D. R. (2021) Spectral resolution and Raman Q^3 and Q^2 cross sections in ~40 mol% Na_2O glasses. *Chem. Geol.* **562**, 120040.

Nesbitt H. W., O'Shaughnessy C., Henderson G. S., Michael Bancroft G. and Neuville D. R. (2019) Factors affecting line shapes and intensities of Q^3 and Q^4 Raman bands of Cs silicate glasses. *Chem. Geol.* **505**, 1–11.

Neuville D., Cormier L., Montouillout V. and Massiot D. (2007) Local Al site distribution in aluminosilicate glasses by ^{27}Al MQMAS NMR. *J. Non-Cryst. Solids* **353**, 180–184.

Neuville D. R. (2006) Viscosity, structure and mixing in (Ca, Na) silicate melts. *Chem. Geol.* **229**, 28–41.

Neuville D. R., Cormier L., de Ligny D., Roux J., Flank A.-M. and Lagarde P. (2008a) Environments around Al, Si, and Ca in aluminate and aluminosilicate melts by X-ray absorption spectroscopy at high temperature. *Am. Mineral.* **93**, 228–234.

Neuville D. R., Cormier L. and Massiot D. (2006) Al coordination and speciation in calcium aluminosilicate glasses: effects of composition determined by ^{27}Al MQ-MAS NMR and Raman spectroscopy. *Chem. Geol.* **229**, 173–185.

Neuville D. R., Cormier L., Montouillout V., Florian P., Millot F., Rifflet J.-C. and Massiot D. (2008b) Structure of Mg- and Mg/Ca aluminosilicate glasses: ^{27}Al NMR and Raman spectroscopy investigations. *Am. Mineral.* **93**, 1721–1731.

Neuville D. R. and Mysen B. O. (1996) Role of aluminium in the silicate network: In situ, high-temperature study of glasses and melts on the join SiO_2-$NaAlO_2$. *Geochim. Cosmochim. Acta* **60**, 1727–1737.

Neuville D. R. and Richet P. (1991) Viscosity and mixing in molten (Ca, Mg) pyroxenes and garnets. *Geochim. Cosmochim. Acta* **55**, 1011–1019.

Oglesby J. V., Zhao P. and Stebbins J. F. (2002) Oxygen sites in hydrous aluminosilicate glasses: the role of Al-O-Al and H_2O. *Geochim. Cosmochim. Acta* **66**, 291–301.

Okuno M., Zotov N., Schmücker M. and Schneider H. (2005) Structure of SiO_2–Al_2O_3 glasses: combined X-ray diffraction, IR and Raman studies. *J. Non-Cryst. Solids* **351**, 1032–1038.

Paduszyński K. and Domańska U. (2014) Viscosity of ionic liquids: an extensive database and a new group contribution model based on a feed-forward artificial neural network. *J. Chem. Inf. Model.* **54**, 1311–1324.

Papale P. (1999) Strain-induced magma fragmentation in explosive eruptions. *Nature* **397**, 425–428.

Park S. Y. and Lee S. K. (2014) High-resolution solid-state NMR study of the effect of composition on network connectivity and structural disorder in multi-component glasses in the diopside and jadeite join: implications for structure of andesitic melts. *Geochim. Cosmochim. Acta* **147**, 26–42.

Paszke A., Gross S., Massa F., Lerer A., Bradbury J., Chanan G., Killeen T., Lin Z., Gimelshein N., Antiga L., Desmaison A., Kopf A., Yang E., DeVito Z., Raison M., Tejani A., Chilamkurthy S., Steiner B., Fang L., Bai J. and Chintala S. (2019) PyTorch: an imperative style, high-performance deep learning library. *Adv. Neural Inf. Process. Syst.* **32**, 8026–8037.

Pedregosa F., Varoquaux G., Gramfort A., Michel V., Thirion B., Grisel O., Blondel M., Prettenhofer P., Weiss R. and Dubourg V., et al. (2011) Scikit-learn: machine learning in Python. *J. Mach. Learn. Res.* **12**, 2825–2830.

Persikov E. S. (1991) The viscosity of magmatic liquids: experiment, generalized patterns. A model for calculation and prediction. Applications. *Adv. Phys. Geochem.* **9**, 1–40.

Rammensee W. and Fraser D. G. (1982) Determination of activities in silicate melts by Knudsen cell mass spectrometry – I. The system $NaAlSi_3O_8$-$KAlSi_3O_8$. *Geochim. Cosmochim. Acta* **46**, 2269–2278.

Rapaport D. C. (2004) *The Art of Molecular Dynamics Simulation*, second ed. Cambridge University Press, Cambridge, U.K..

Richet P. (1987) Heat capacity of silicate glasses. *Chem. Geol.* **62**, 111–124.

Richet P. (1984) Viscosity and configurational entropy of silicate melts. *Geochim. Cosmochim. Acta* **48**, 471–483.

Richet P. and Bottinga Y. (1984) Glass transitions and thermodynamic properties of amorphous SiO_2, $NaAlSi_nO_{2n+2}$ and $KAlSi_3O_8$. *Geochim. Cosmochim. Acta* **48**, 453–470.

Richet P. and Bottinga Y. (1985) Heat capacity of aluminum-free liquid silicates. *Geochim. Cosmochim. Acta* **49**, 471–486.

Riebling E. F. (1966) Structure of sodium aluminosilicate melts containing at least 50 mol% SiO_2 at 1500°C. *J. Chem. Phys.* **44**, 2857–2865.

Robert G., Smith R. A. and Whittington A. G. (2019) Viscosity of melts in the $NaAlSiO_4$-$KAlSiO_4$-SiO_2 system: configurational entropy modelling. *J. Non-Cryst. Solids* **524**, 119635.

Robert G., Whittington A. G., Stechern A. and Behrens H. (2013) The effect of water on the viscosity of a synthetic calc-alkaline basaltic andesite. *Chem. Geol.* **346**, 135–148.

Russell J. K. and Giordano D. (2017) Modelling configurational entropy of silicate melts. *Chem. Geol.* **461**, 140–151.

Russell J. K., Giordano D. and Dingwell D. B. (2003) High-temperature limits on viscosity of non-Arrhenian silicate melts. *Am. Mineral.* **88**, 1390–1394.

Sakka S. and MacKenzie J. D. (1971) Relation between apparent glass transition temperature and liquids temperature for inorganic glasses. *J. Non-Cryst. Solids* **6**, 145–162.

Schairer J. F. and Bowen N. L. (1955) The system K_2O-Al_2O-SiO_2. *Am. J. Sci.* **253**, 681–746.

Schairer J. F. and Bowen N. L. (1956) The system Na_2O-Al_2O-SiO_2. *Am. J. Sci.* **254**, 129–195.

Scherer G. W. (1984) Use of the adam-gibbs equation in the analysis of structural relaxation. *J. Am. Ceram. Soc.* **67**, 504–511.

Secrist D. R., MacKenzie J. D., Lee E. H. and Rogers T. G. (1965) Identification of uncommon noncrystalline solids as glasses. *J. Am. Ceram. Soc.* **48**, 487–491.

Sehlke A. and Whittington A. G. (2016) The viscosity of planetary tholeiitic melts: a configurational entropy model. *Geochim. Cosmochim. Acta* **191**, 277–299.

Seifert F., Mysen B. O. and Virgo D. (1982) Three-dimensional network structure of quenched melts (glass) in the systems SiO_2-$NaAlO_2$, SiO_2-$CaAl_2O_4$ and SiO_2-$MgAl_2O_4$. *Am. Mineral.* **67**, 696–717.

Sen P. N. and Thorpe M. F. (1977) Phonons in AX_2 glasses: from molecular to band-like modes. *Phys. Rev. B* **15**, 4030–4038.

Shaw H. R. (1972) Viscosities of magmatic silicate liquids: an empirical method of prediction. *Am. J. Sci.* **272**, 870–893.

Smith J. D., Azizzadenesheli K. and Ross Z. E. (2020) EikoNet: solving the eikonal equation with deep neural networks. *IEEE Trans. Geosci. Remote Sens.*, 1–12.

Snoek J., Larochelle H. and Adams R. P. (2012) Practical bayesian optimization of machine learning algorithms. *ArXiv12062944 Cs Stat.*.

Sreenivasan H., Kinnunen P., Adesanya E., Patanen M., Kantola A. M., Telkki V.-V., Huttula M., Cao W., Provis J. L. and Illikainen M. (2020) Field strength of network-modifying cation dictates the structure of (Na-Mg) aluminosilicate glasses. *Front. Mater.* **7**, 267.

Srivastava N., Hinton G., Krizhevsky A., Sutskever I. and Salakhutdinov R. (2014) Dropout: a simple way to prevent neural networks from overfitting. *J. Mach. Learn. Res.* **15**, 1929–1958.

Starodub K., Wu G., Yazhenskikh E., Müller M., Khvan A. and Kondratiev A. (2019) An Avramov-based viscosity model for the SiO_2-Al_2O_3-Na_2O-K_2O system in a wide temperature range. *Ceram. Int.* **45**, 12169–12181.

Stebbins J. F., Carmichael I. S. E. and Moret L. K. (1984) Heat capacities and entropies of silicate liquids and glasses. *Contrib. Miner. Petrol.* **86**, 131–148.

Stebbins J. F., Dubinsky E. V., Kanehashi K. and Kelsey K. E. (2008) Temperature effects on non-bridging oxygen and aluminum coordination number in calcium aluminosilicate glasses and melts. *Geochim. Cosmochim. Acta* **72**, 910–925.

Stebbins J. F., Kroeker S., Lee S. K. and Kiczenski T. J. (2000) Quantification of five- and six-coordinated aluminum ions in aluminosilicate and fluoride-containing glasses by high-field, high-resolution ^{27}Al NMR. *J. Non-Cryst. Solids* **275**, 1–6.

Stebbins J. F., Lee S. K. and Oglesby J. V. (1999) Al-O-Al oxygen sites in crystalline aluminates and aluminosilicate glasses; high-resolution oxygen-17 NMR results. *Am. Mineral.* **84**, 983–986.

Stebbins J. F. and Xu Z. (1997) NMR evidence for excess non-bridging oxygen in an aluminosilicate glass. *Nature* **390**, 60–62.

Tandia A., Onbasli M. C. and Mauro J. C. (2019) Machine Learning for Glass Modeling. In *Springer Handbook of Glass* (eds. J. D. Musgraves, J. Hu and L. Calvez). Springer Handbooks. Springer International Publishing, Cham, pp. 1157–1192.

Tangeman J. A. and Lange R. A. (1998) The effect of Al^{3+}, Fe^{3+}, and Ti^{4+} on the configurational heat capacities of sodium silicate liquids. *Physic Chem. Miner.* **26**, 83–99.

Taylor T. D. and Rindone G. E. (1970) Properties of soda aluminosilicate glasses: V, low-temperature viscosities. *J. Am. Ceram. Soc.* **53**, 692–695.

Thompson L. M. and Stebbins J. F. (2013) Interaction between composition and temperature effects on non-bridging oxygen and high-coordinated aluminum in calcium aluminosilicate glasses. *Am. Mineral.* **98**, 1980–1987.

Thompson L. M. and Stebbins J. F. (2011) Non-bridging oxygen and high-coordinated aluminum in metaluminous and peraluminous calcium and potassium aluminosilicate glasses: high-resolution ^{17}O and ^{27}Al MAS NMR results. *Am. Mineral.* **96**, 841–853.

Thompson L. M. and Stebbins J. F. (2012) Non-stoichiometric non-bridging oxygens and five-coordinated aluminum in alkaline earth aluminosilicate glasses: effect of modifier cation size. *J. Non-Cryst. Solids* **358**, 1783–1789.

Toplis M. J. (1998) Energy barriers to viscous flow and the prediction of glass transition temperatures of molten silicates. *Am. Mineral.* **83**, 480–490.

Toplis M. J., Dingwell D. B., Hess K.-U. and Lenci T. (1997a) Viscosity, fragility, and configurational entropy of melts along the join SiO_2-$NaAlSiO_4$. *Am. Mineral.* **82**, 979–990.

Toplis M. J., Dingwell D. B. and Lenci T. (1997b) Peraluminous viscosity maxima in Na_2O-Al_2O_3-SiO_2 liquids: the role of triclusters in tectosilicate melts. *Geochim. Cosmochim. Acta* **61**, 2605–2612.

Toplis M. J., Kohn S. C., Smith M. E. and Poplett J. F. (2000) Fivefold-coordinated aluminum in tectosilicate glasses observed by triple quantum MAS NMR. *Am. Mineral.* **85**, 1556–1560.

Urbain G., Bottinga Y. and Richet P. (1982) Viscosity of liquid silica, silicates and alumino-silicates. *Geochim. Cosmochim. Acta* **46**, 1061–1072.

Varshneya A. K. and Bihuniak P. P. (2017) Cover screens for personal electronic devices: strengthened glass or sapphire? *Am. Ceram. Soc. Bull.* **96**, 6.

Villemant B. and Boudon G. (1998) Transition from dome-forming to plinian eruptive styles controlled by H_2O and Cl degassing. *Nature* **392**, 65–69.

Virgo D., Mysen B. O. and Kushiro I. (1980) Anionic constitution of 1-Atmosphere silicate melts: implications for the structure of igneous melts. *Science* **208**, 1371–1373.

Vuilleumier R., Sator N. and Guillot B. (2009) Computer modeling of natural silicate melts: what can we learn from ab initio simulations. *Geochim. Cosmochim. Acta* **73**, 6313–6339.

Wang Y., Sakamaki T., Skinner L. B., Jing Z., Yu T., Kono Y., Park C., Shen G., Rivers M. L. and Sutton S. R. (2014) Atomistic insight into viscosity and density of silicate melts under pressure. *Nat. Commun.* **5**, 3241.

Webb S. L. L. (2008) Configurational heat capacity of Na_2O–CaO–Al_2O–SiO_2 melts. *Chem. Geol.* **256**, 92–101.

Willard J., Jia X., Xu S., Steinbach M. and Kumar V. (2020) Integrating physics-based modeling with machine learning: a survey. *ArXiv200304919 Phys Stat.*.

Xiang Y., Du J., Smedskjaer M. M. and Mauro J. C. (2013) Structure and properties of sodium aluminosilicate glasses from molecular dynamics simulations. *J. Chem. Phys.* **139**, 044507.

You J.-L., Jiang G.-C., Hou H.-Y., Chen H., Wu Y.-Q. and Xu K.-D. (2005) Quantum chemistry study on superstructure and Raman spectra of binary sodium silicates. *J. Raman Spectrosc.* **36**, 237–249.

Zakaznova-Herzog V. P., Malfait W. J., Herzog F. and Halter W. E. (2007) Quantitative Raman spectroscopy: principles and application to potassium silicate glasses. *J. Non-Cryst. Solids* **353**, 4015–4028.

Associate editor: Sung Keun Lee